

Precessing Black Hole Jets and Galactic Fossils

María J. Rodríguez^{1,2,*}

¹*Department of Physics, Utah State University,
4415 Old Main Hill Road, Logan, UT 84322, USA*

²*Instituto de Física Teórica UAM-CSIC,
Universidad Autónoma de Madrid, 28049 Madrid, Spain*

* majo.rodriguez.b@gmail.com

Abstract

The Galactic Centre gamma-ray excess (GCE) — an anomalous $\sim 2\text{--}5$ GeV signal detected by *Fermi*-LAT around Sgr A* — has remained without a consensus interpretation for more than fifteen years. Dark-matter annihilation and unresolved millisecond-pulsar populations remain the leading candidates, yet neither incorporates the past activity of Sgr A* recorded by the Fermi and eROSITA bubbles (FEB). We propose a unified scenario in which both the GCE and the FEB are fossil imprints of a single past episode of Sgr A* activity: a precessing parabolic Blandford–Znajek black-hole jet launched from a tilted, magnetically arrested accretion disc during a ~ 7.5 Myr active phase ending ~ 2.6 Myr ago. In this picture, the jet both inflated the observed kpc-scale FEB and injected hadronic cosmic rays that contribute to the GCE flux. The model rests on three independently motivated physical inputs: the EHT-proposed $\sim 35^\circ$ tilt of the Sgr A* spin axis from the Galactic rotation axis, Lense–Thirring precession of the misaligned disc through ~ 5 azimuthal cycles during the active phase, and a two-zone cosmic-ray transport prescription through the CMZ and bulge anchored to standard inner-Galaxy diffusion coefficients. We verify the model’s internal consistency by checking that the proton Larmor radius along the jet column is small enough to magnetically confine the cosmic-ray population and that the gamma-ray optical depth toward the Galactic Centre is negligible, leaving the interstellar medium transparent to the produced photons. Comparison with current GCE observations yields a spin-dependent hadronic contribution. For the EHT-favoured Sgr A* spin $a_* = 0.9$, we find an irreducible hadronic floor of $\sim 3\text{--}14\%$ of the observed GCE surface brightness across the inner ten degrees, highlighting a previously unexplored component relevant for comprehensive models of the GCE.

Contents

1	Introduction	2
2	The Physical Model	4
2.1	Black-hole and jet parameters	5
2.2	Magnetic field profile and horizon field	7
2.3	Jet geometry: tilt and Lense–Thirring precession	10
2.4	Precession-averaged CR injection fraction	11
2.5	Bubble dynamics: Sedov–Taylor expansion	12
2.6	Hadronic gamma-ray luminosity and the GCE budget	13
3	Derivation of the Hadronic Gamma-Ray Surface Brightness	16
3.1	Volume emissivity from $pp \rightarrow \pi^0 \rightarrow \gamma\gamma$	16
3.2	Isotropic CR cloud approximation	17
3.3	Two-zone CR diffusion Green function	18
3.4	Line-of-sight integral and surface brightness	20
3.5	Energy-resolved spectrum: leaky-box treatment	22
3.6	Caveats of the spatial–spectral factorisation	22
4	Galactic Spectrum and Brightness	23
5	Triaxial bar gas and longitudinal asymmetry	26
5.1	The asymmetry decomposition	26
5.2	Asymmetry profile	27
5.3	Discriminating among GCE scenarios	28
6	Conclusions	29
A	Magnetic Field Configuration	31
A.1	Vector Potential	32
A.2	Angular Structure and Magnetic Components	33
A.3	Connection to the Blandford–Znajek Power	33
A.4	Validity of the Force-Free Approximation	34
B	Multipole analysis of the diffusion equation	34

1. Introduction

The *Fermi* Large Area Telescope revealed an excess of $\sim 2\text{--}5$ GeV gamma-ray emission centred on the Galactic Centre, extending over $\sim 10^\circ$ (~ 1.5 kpc) and approximately spherically symmetric about Sgr A* [1, 2, 3, 4]. This Galactic Centre Excess (GCE) has a spectrum peaking near $E_\gamma \simeq 2$ GeV and a morphology compatible with a generalised NFW² profile of slope $\gamma \simeq 1.2\text{--}1.3$ [5, 6], making it one of the most discussed anomalies in high-energy astrophysics. Two primary interpretations have dominated the literature: the dark-matter (DM) annihilation hypothesis [1, 2, 4, 5], attributing the excess to $\sim 40\text{--}60$ GeV WIMPs annihilating primarily to $b\bar{b}$, and the unresolved millisecond-pulsar (MSP) hypothesis [7, 8, 9, 10, 11], which notes that the GCE spectrum is nearly indistinguishable from a superposition of MSP spectra sourced by the bulge stellar population. Both face challenges: the DM hypothesis requires a fine-tuned cusp in the presence of the Galactic bar, while the MSP hypothesis requires MSPs $\gtrsim 5\times$ less luminous than their disc counterparts to satisfy point-source count constraints.

A fundamental limitation common to both interpretations is that neither incorporates the past activity of Sgr A* directly recorded by the Fermi and eROSITA bubbles (FEB or Fermi/eROSITA). These giant γ -ray and X-ray lobes, extending $\sim 8\text{--}14$ kpc above and below the Galactic plane and highly symmetric about the disc and rotation axis [12, 13, 14], provide compelling evidence that Sgr A* underwent a major energetic outburst within the past ~ 10 Myr. Cosmological simulations indicate that such structures are generic to disc galaxies of this mass: two-thirds of the 198 Milky Way/M31 analogues in TNG50 host comparable circumgalactic X-ray bubbles attributed to episodic SMBH-driven outbursts [15]. The most directly relevant simulation work for our case is that of Yang, Ruszkowski & Zweibel [16], whose magneto-hydrodynamic (MHD) modelling of FEB inflation by past Sgr A* jet activity establishes the $\sim 7\text{--}10$ Myr active duration and ~ 2.6 Myr time since shutoff, of which we adopt $T_{\text{act}} = 7.5$ Myr as fiducial. Such simulations, however, treat the Sgr A* jet as static and axially aligned with the Galactic rotation axis — leaving unincorporated the $\sim 35^\circ$ tilt of the Sgr A* spin axis with respect to the Galactic plane now indicated by EHT polarimetry [17, 18].

In this paper we propose that a *precessing* parabolic Blandford–Znajek (BZ) jet [19] from Sgr A* during its past active phase both inflated the Fermi/eROSITA bubbles and injected hadronic cosmic-ray (CR) protons into the inner Galaxy, producing GCE-relevant gamma-ray emission via inelastic pp collisions [20, 21]. This generalises the static-jet picture of Yang et al. [16] by incorporating the EHT-measured spin-axis tilt: Lense–Thirring precession of the misaligned disc averages the otherwise off-axis CR injection into a quasi-spherical pattern compatible with the observed GCE morphology, simultaneously unifying the EHT tilt, the FEB inflation, and the GCE residual into a single self-consistent picture of Sgr A*'s recent activity. To our knowledge, no prior FEB or GCE model has folded the precessing-jet geometry into the resulting CR injection. The interpretation rests on a specific observational tension that the precessing-jet geometry resolves: a static jet on the tilted axis would produce an asymmetric, off-axis CR injection incompatible with the nearly-spherical GCE, while Lense–Thirring precession sweeps the BZ injection cone azimuthally over the active phase to recover the observed morphology.

The BZ mechanism, central to our proposal, sits within a broader theoretical landscape of energy-extraction processes from rotating black holes, sometimes referred to more broadly as superradiance. The original Penrose process [22, 23] demonstrated that the

rotational energy of a Kerr black hole can in principle be tapped through orbits within the ergosphere; astrophysically relevant variants include superradiant amplification of bosonic fields [24, 25, 26, 27], gravitational-wave-driven extraction in binary mergers [28], and electromagnetic energy extraction by the BZ mechanism [19, 29, 30, 31, 32]. Numerical simulations of magnetically arrested accretion confirm that BZ extraction can convert a substantial fraction of the black-hole rotational energy into a Poynting-dominated jet [33, 34, 35, 36, 37], with conversion efficiency η_{BZ} approaching unity for $a_* \gtrsim 0.9$ and saturated horizon flux. We adopt $\eta_{\text{BZ}} \simeq 1.0$ at MAD saturation; the resulting jet power and total energy budget are derived in Sec. 2.1.

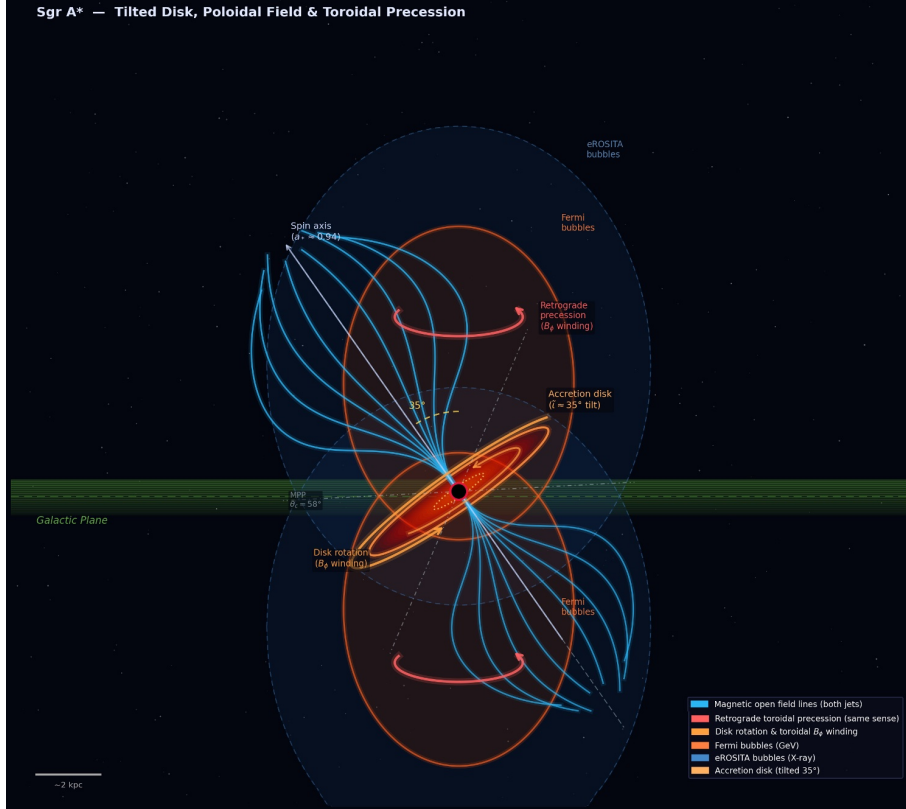


Figure 1: Schematic of the proposed model. The accretion disk (orange ellipse), tilted by $i_{\text{tilt}} \simeq 35^\circ$ from the Galactic plane (green band), launches a parabolic Blandford–Znajek jet within a critical cone of half-angle $\theta_c \simeq 20^\circ$ from the spin axis (dashed grey lines) [38]. Open poloidal field lines (cyan) thread the polar caps. Lense–Thirring precession (red arrows) sweeps the spin axis azimuthally with period $T_{\text{prec}} \simeq 1.6$ Myr over the active phase $T_{\text{act}} \simeq 7.5$ Myr, averaging the cosmic-ray injection into a quasi-spherical pattern. The Fermi (orange-red lobes) and eROSITA (blue dashed ellipses) bubbles are interpreted as fossil evidence of this outburst [12, 13, 16]. The dashed blue line indicates the spin axis ($a_* \simeq 0.9$); the gold arc marks the 35° tilt angle.

Three physical inputs, each independently constrained by observations, conspire to reproduce the GCE morphology without free-parameter tuning beyond the active duration T_{act} : (i) a permanent tilt of $i_{\text{tilt}} \simeq 35^\circ$ between the Sgr A* spin axis and the Galactic plane, constrained by EHT polarimetry [17, 18] and incorporated into recent MHD simulations of jet-driven bubble inflation [16, 39]; (ii) Lense–Thirring precession of the tilted accretion disk, which sweeps the BZ jet cone over a full azimuthal circle with period $T_{\text{prec}} \simeq 1.6$ Myr, averaging the CR injection into a quasi-spherical pattern — a

precession-averaging mechanism developed here; and (iii) a two-zone cosmic-ray transport prescription through the CMZ and bulge anchored to standard inner-Galaxy diffusion coefficients, which redistributes the injected protons over a length scale $\lambda_{\text{diff}} \simeq 1.73$ kpc matching the observed GCE half-width. Our main claim is *not* that the BZ mechanism explains *all* of the GCE; rather, that for the EHT-favoured high spin $a_\star = 0.9$ it produces an irreducible hadronic floor at the $\sim 3\text{--}14\%$ level of the GCE surface brightness across $\theta \in [0.5^\circ, 10^\circ]$ in the 1–10 GeV band, additive to any fraction arising from DM or MSPs and bounded morphologically rather than energetically by the diffusion-broadened profile. The contribution falls to the percent level at $a_\star \lesssim 0.5$, making the floor strongly spin-dependent. Any complete GCE model may need to account for this floor.

The paper is structured as follows. Section 2 describes the physical model and all parameter choices, with the full fiducial parameter set collected in Table 2. Section 3 presents the analytic derivation of the hadronic gamma-ray surface brightness, introducing the isotropic CR-cloud approximation, computing the two-zone diffusion Green function, and integrating along the line of sight to obtain the energy-resolved spectrum. Section 4 compares the results against current GCE measurements through χ^2 fits to the angular profile, identifies the obstacles to a BZ-only origin, and positions the model relative to prior FEB and GCE work. Section 5 develops the triaxial-bar upgrade to the gas density and the resulting peaked longitudinal asymmetry as a categorical observational discriminator. Section 6 summarises our results, places them in the context of M87 as an active-AGN benchmark, and discusses consistency with present-day observations of Sgr A[∗] and the inner Galaxy. Appendix A collects the analytical structure of the BZ magnetic field, its connection to the BZ jet power, and the validity of the force-free approximation. Appendix B presents the formal multipole analysis of the diffusion equation that justifies the isotropic-cloud approximation used in the main text.

2. The Physical Model

We model Sgr A[∗] as a magnetically-dominated, sub-Eddington source that drives both the Fermi/eROSITA bubbles and the GCE through three coupled processes: (i) a precessing parabolic Blandford–Znajek (BZ) jet depositing hadronic CRs within a polar cone; (ii) Lense–Thirring precession of a tilted accretion disc sweeping that cone over the full azimuth; (iii) two-zone CR diffusion redistributing the injection into a morphology matching the observed GCE. Each ingredient is independently constrained by observation; the combination determines a bubble geometry, the GCE spatial profile, and an irreducible hadronic floor without free-parameter tuning beyond the active duration T_{act} .

The black-hole and jet-power parameters are summarised in Sec. 2.1; the horizon-scale magnetic field is derived in Sec. 2.2, with the full vector potential given in Appendix A; the jet geometry, tilt and Lense–Thirring precession are treated in Sec. 2.3; the precession-averaged CR injection fraction is derived in Sec. 2.4; bubble dynamics in Sec. 2.5; and the resulting hadronic gamma-ray budget in Sec. 2.6. The geometry of the model — including the spin-axis tilt i_{tilt} , the BZ cone half-angle θ_c , the precession circle, the accretion disc orientation, and the line-of-sight angles θ and ϑ entering the surface-brightness integral of Sec. 3 — is summarised in Fig. 2, to which we refer throughout.

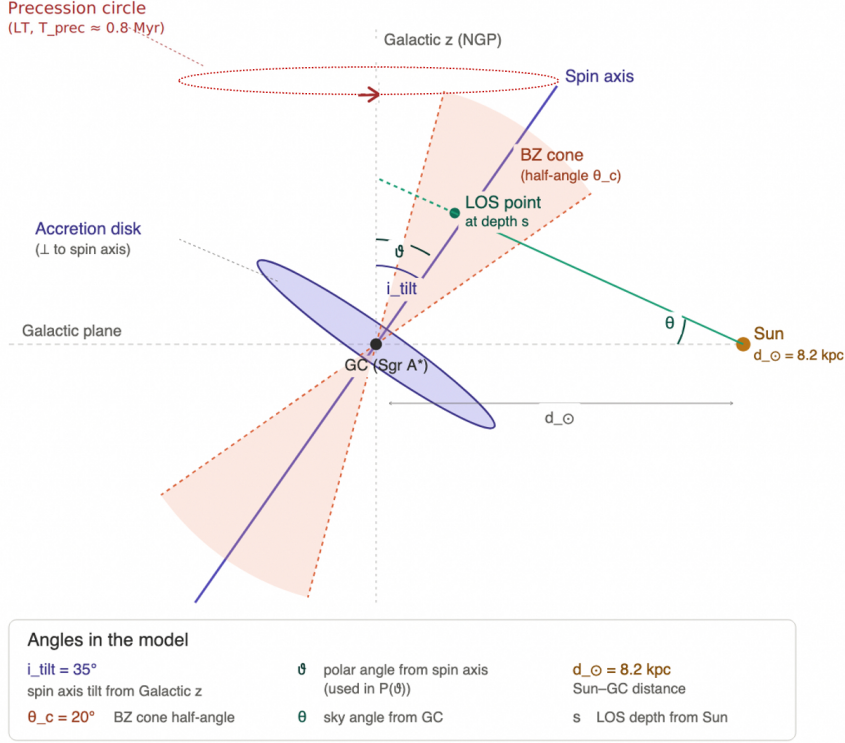


Figure 2: Horizon-scale geometry of the precessing BZ jet from Sgr A^{*}. The spin axis (purple, dashed) is tilted by $i_{\text{tilt}} \simeq 35^\circ$ from the Galactic \hat{z} -axis (vertical, NGP), corresponding to the EHT-inferred line-of-sight inclination $i \simeq 150^\circ$ [18]. The accretion disc (purple ellipse) lies perpendicular to the spin axis; the BZ critical cone (orange wedge) is launched with half-angle $\theta_c \simeq 20^\circ$ around the instantaneous spin axis. The Lense–Thirring precession circle (red dashed ellipse) traces the spin-axis tip around the Galactic \hat{z} -axis with period $T_{\text{prec}} \simeq 1.6 \text{ Myr}$. The polar angle ϑ (from Galactic \hat{z}) and sky angle θ (from the Sun–GC line of sight) entering Eq. (23) and the surface-brightness integral of Sec. 3 are indicated.

2.1 Black-hole and jet parameters

Sgr A^{*} is modelled as a Kerr black hole of mass $M_\bullet = 4.15 \times 10^6 M_\odot$ [40] and dimensionless spin $a_\star = 0.9$, consistent with the outflow-method analysis of [41] ($a_\star = 0.90 \pm 0.06$) and the EHT 2024 polarimetric best-bet model [18] ($a_\star = 0.94$, MAD, $i = 150^\circ$). The accretion flow is geometrically thick and radiatively inefficient — an ADAF [42, 43] — appropriate for the inferred sub-Eddington accretion rate. Such flows efficiently advect large-scale poloidal magnetic flux inward without radiative dissipation; over the $\sim 7.5 \text{ Myr}$ active phase we assume this flux accumulates at the horizon until magnetic pressure approaches the ram pressure of infalling gas — the magnetically arrested disc (MAD) state [33, 34]. The gravitational and event-horizon radii are

$$r_g = \frac{GM_\bullet}{c^2} = 6.12 \times 10^{11} \text{ cm}, \quad r_+ = r_g \left(1 + \sqrt{1 - a_\star^2} \right) = 1.44 r_g, \quad (1)$$

giving horizon angular velocity

$$\Omega_H = \frac{a_\star c}{2r_+} = 1.54 \times 10^{-2} \text{ rad s}^{-1}. \quad (2)$$

The Eddington luminosity is

$$L_{\text{Edd}} = 1.26 \times 10^{38} \frac{M_{\bullet}}{M_{\odot}} \text{ erg s}^{-1} = 5.23 \times 10^{44} \text{ erg s}^{-1}, \quad (3)$$

with corresponding Eddington accretion rate $\dot{M}_{\text{Edd}} \equiv L_{\text{Edd}}/(0.1 c^2) \simeq 0.092 M_{\odot} \text{ yr}^{-1}$ (assuming a fiducial radiative efficiency $\eta_{\text{rad}} = 0.1$). During the active phase $\dot{m} \equiv \dot{M}/\dot{M}_{\text{Edd}} = 1 \times 10^{-5}$ is fixed, representing a $\sim 10^3$ enhancement over the present-day quiescent value $\dot{m}_{\text{today}} \sim 10^{-8}$ [44, 43] and comparable to the present-day accretion rate of M87 [45, 43]. The corresponding accretion rate is $\dot{M} \simeq 9.2 \times 10^{-7} M_{\odot} \text{ yr}^{-1}$.

The BZ jet power is given by the standard relation [19, 33]

$$P_{\text{BZ}} = \eta_{\text{BZ}} \dot{M} c^2 = \eta_{\text{BZ}} \dot{m} \dot{M}_{\text{Edd}} c^2, \quad (4)$$

where η_{BZ} is the dimensionless BZ efficiency. The BZ efficiency

$$\eta_{\text{BZ}}(a_*) \propto \Omega_H^2 (1 + 1.38 \Omega_H^2 - 9.2 \Omega_H^4) \quad (5)$$

follows the Tchekhovskoy, Narayan & McKinney [33] MAD scaling. For a high-spin ($a_* = 0.9$) black hole at MAD saturation, GRMHD simulations give $\eta_{\text{BZ}} \simeq 1.0$ [33, 34]. With the fiducial $\dot{m} = 10^{-5}$, this yields

$$P_{\text{BZ}} \simeq 5.2 \times 10^{40} \text{ erg s}^{-1}, \quad (6)$$

which lies a factor of ~ 2 below the time-averaged mechanical-luminosity bound $\lesssim 10^{41} \text{ erg s}^{-1}$ derived from the O VIII/O VII line ratio toward the Fermi/eROSITA bubbles [46, 47].¹

The total injected jet energy over the fiducial active duration $T_{\text{act}} = 7.5 \text{ Myr}$ [16] is

$$E_{\text{jet}} = P_{\text{BZ}} T_{\text{act}} \approx 1.2 \times 10^{55} \text{ erg}, \quad (7)$$

representing ~ 10 – 15% of the total Fermi/eROSITA bubble energy budget of $\sim 10^{56} \text{ erg}$ [12, 13, 16]; the remainder is contributed by accretion-disc winds [48] and possibly a sequence of Tidal Disruption Event (TDE)-driven outflows [49, 50].

In contrast to the disc inclination and accretion rate, the BH spin is essentially frozen over the timescales relevant to this work. The fractional mass — and hence spin — change over the active phase is

$$\frac{\Delta a_*}{a_*} \lesssim \frac{\Delta M_{\bullet}}{M_{\bullet}} = \frac{\dot{M} \cdot T_{\text{act}}}{M_{\bullet}} \sim \frac{10^{-6} \times 7.5 \times 10^6}{4.15 \times 10^6} \sim 2 \times 10^{-6}. \quad (8)$$

This is entirely negligible. The spin is considered effectively constant between the active phase and today, making it the most robustly fixed physical parameter in the model.

¹For a more conservative spin $a_* = 0.5$, the MAD efficiency drops to $\eta_{\text{BZ}} \simeq 0.18$, giving $P_{\text{BZ}} \simeq 9.3 \times 10^{39} \text{ erg s}^{-1}$ and $E_{\text{jet}} \simeq 2.2 \times 10^{54} \text{ erg}$ at the same $\dot{m} = 10^{-5}$, both a factor ~ 5 below the high-spin fiducial. Increasing \dot{m} to 5×10^{-5} at $a_* = 0.5$ would recover comparable energetics but requires accretion at the upper end of the sub-Eddington range disfavored by existing bounds [46].

2.2 Magnetic field profile and horizon field

The horizon magnetic field strength is set by the steady-state MAD saturation condition. In the magnetically arrested disc state [33, 34], large-scale poloidal flux accumulates at the BH horizon until magnetic stresses periodically arrest the accretion inflow. The saturation level is characterised by the dimensionless horizon flux

$$\phi \equiv \frac{\Phi_{\text{BH}}}{\sqrt{\dot{M} c r_g^2}} \simeq 50, \quad (9)$$

where $\Phi_{\text{BH}} = \int_H \mathbf{B} \cdot d\mathbf{A}$ is the poloidal flux threading one hemisphere of the horizon [33]. The horizon flux Φ_{BH} is determined by the BZ jet power through the Blandford–Znajek relation

$$P_{\text{BZ}} = \kappa \frac{\Omega_H^2 \Phi_{\text{BH}}^2}{4\pi c}, \quad (10)$$

with BZ geometric coefficient $\kappa \simeq 0.045$ for dimensionless black hole spin $a_* = 0.9$ [33, 34]. Inverting Eq. (10) for the chosen jet power P_{BZ} fixes the active-phase horizon flux, and hence the field

$$B_H^{(0)} \equiv \frac{\Phi_{\text{BH}}}{\pi r_+^2} = \frac{1}{\pi r_+^2} \sqrt{\frac{4\pi c P_{\text{BZ}}}{\kappa \Omega_H^2}} \simeq 2 \times 10^4 \text{ G}, \quad (11)$$

where $r_+ = (1 + \sqrt{1 - a_*^2}) r_g$ is the horizon radius and $\Omega_H = a_* c / (2r_+)$ is the horizon angular velocity. The MAD condition (9) is then satisfied for an accretion rate $\dot{M} = \Phi_{\text{BH}}^2 / (\phi^2 c r_g^2)$, corresponding to $\dot{m} \equiv \dot{M} / \dot{M}_{\text{Edd}} \simeq 10^{-5}$ and BZ efficiency $\eta_{\text{BZ}} \equiv P_{\text{BZ}} / (\dot{M} c^2) \simeq 1.0$.

Although Eq. (9) is conventionally referred to as “magnetic pressure balancing the ram pressure of infall,” the actual saturation level departs from naive pressure equality by an order of magnitude. Plugging in our active-phase parameters, the horizon magnetic pressure is

$$P_B = \frac{B_H^{(0)2}}{8\pi} \simeq 1.6 \times 10^7 \text{ erg cm}^{-3}, \quad (12)$$

while the inflow ram-pressure scale

$$P_{\text{ram}} \equiv \rho v^2 = \frac{\dot{M} c}{4\pi r_g^2} \simeq 4 \times 10^5 \text{ erg cm}^{-3}. \quad (13)$$

We evaluate the spherical inflow limit. The ram pressure expression evaluates the cross-sectional area at the gravitational radius r_g instead of the horizon radius r_+ . Substituting r_+ decreases the pressure by a factor of $(r_+/r_g)^{-2} \simeq 0.48$.

This confirms the validity of the magnetically arrested saturation condition. The ratio $P_B / P_{\text{ram}} \sim 40$ is the standard MAD-saturation value [33], equivalent to the dimensionless flux $\phi \simeq 50$ of Eq. (9). The factor ~ 40 rather than ~ 1 reflects that the magnetic field obstructs accretion only in the polar regions while equatorial inflow continues intermittently — the field need not arrest the entire flow at all latitudes, only enough of the polar inflow to throttle mass supply on the dynamical timescale. Periodic flux eruptions release accumulated field as the inflow temporarily resumes, leaving the time-averaged flux at $\phi \simeq 50$ in steady state.

The field $B_H^{(0)}$ in Eq. (11) is the active-phase value during the FEB-driving outburst at $\dot{m} \sim 10^{-5}$. The MAD scaling $B \propto \sqrt{\dot{m}}$ links this to the present-day quiescent field of ~ 10 – 50 G inferred by the EHT [18] at the current $\dot{m} \sim 10^{-8}$, consistent with the same

MAD branch operating across the active and quiescent epochs. The same scaling links the active-phase field to the present-day horizon field of M87 at $\dot{m} \sim 10^{-5}$ [45, 43], with the residual factor coming from BH mass: $B_H^{\text{SgrA}^*}/B_H^{\text{M87}} \simeq \sqrt{M_{\text{M87}}/M_{\text{SgrA}^*}} \simeq 40$, a kinematic consequence of the MAD criterion applied to two BHs of different mass at comparable accretion rate. No special transient configurations are required.

Comparison with present-day quiescent Sgr A*. The active-phase $B_H^{(0)}$ is roughly three orders of magnitude larger than the horizon-scale field of the present-day quiescent state, $B_{H,\text{today}} \sim 10\text{--}50$ G, inferred from sub-mm SED modelling [51, 44], EHT polarimetry [17, 18], and JWST/MIRI flare observations [52]. The MAD scaling $B_H \propto \sqrt{\dot{m}}$ predicts a ~ 30 -fold enhancement for the inferred $\sim 10^3$ -fold accretion-rate increase between the quiescent ($\dot{m} \sim 10^{-8}$) and active ($\dot{m} \sim 10^{-5}$) phases; the additional factor of ~ 20 is consistent with the present-day flow being below MAD saturation ($\phi_{\text{today}} \ll \phi_{\text{MAD}}$), naturally producing a quiescent jet much weaker than its MAD-state ancestor.

Two cone scales. The model contains two physically distinct cone angles, neither of which should be confused with the other. $\theta_c = 20^\circ$ is the *horizon-scale BZ critical cone* [53, 38] where electromagnetic energy extraction operates; it determines the precession-averaged CR injection fraction $P(\vartheta)$ in Eq. (23) and hence the morphological implication of Sec. 3. $\theta_{\text{open}} \simeq 5^\circ$ is the *asymptotic post-collimation opening half-angle* of the jet spine; it sets the spine cross-section $\pi(R_{\text{bub}} \tan \theta_{\text{open}})^2$ at the bubble wall and hence the equipartition field B_{wall} in Eq. (18) below.

Jet structural transition. Beyond the horizon the jet propagates along parabolic flux surfaces, with the field decreasing as $B(s) \propto s^{-1/2}$ along the jet [19, 54]. Parabolic collimation persists until the magnetic-to-kinetic conversion radius s_{break} , beyond which the jet transitions to a free-flowing conical spine with asymptotic opening angle θ_{open} . The break radius is set by the location where the lateral magnetic pressure of the parabolic jet equals the ambient pressure of the disc-driven wind. We adopt the structure resolved in M87 [55], where VLBI observations locate this transition at $\simeq 10^5 r_g$ with asymptotic opening half-angle $\simeq 5^\circ$, and apply the same scaling to Sgr A*:

$$s_{\text{break}} \simeq 10^5 r_g \simeq 0.02 \text{ pc}, \quad \theta_{\text{open}} \simeq 5^\circ. \quad (14)$$

GRMHD simulations show that the parabolic-to-conical transition is smoothed over \sim a decade in radius rather than being sharp [56, 57], which we approximate by a single break for analytic tractability.

Following the canonical AGN-jet morphology [58, 59, 55], we choose the hybrid collimation profile

$$B(s) = \begin{cases} B_H^{(0)} \left(\frac{r_+}{s}\right)^{3/4} & s \leq s_{\text{break}} \quad (\text{parabolic, force-free}), \\ B_{\text{jet}}(s \tan \theta_{\text{open}}) \propto s^{-1} & s > s_{\text{break}} \quad (\text{conical, equipartition}), \end{cases} \quad (15)$$

where s is the local jet coordinate measured along the spin axis from r_+ outward (distinct from the Galactic \hat{z} -axis), $B_H^{(0)} \simeq 2 \times 10^4$ G from Eq. (11), and $B_{\text{jet}}(r_\perp)$ is the spine equipartition field of Eq. (16) below.

Magnetic-to-kinetic transition at the break. The two regimes in Eq. (15) describe physically different jet phases. Inside s_{break} the jet is *magnetically-dominated* and the field follows the flux-conserving parabolic scaling $B \propto s^{-3/4}$. Beyond s_{break} the jet has converted most of its electromagnetic energy into bulk kinetic energy [60, 35], and the residual magnetic energy density is set by spine equipartition [Eq. (16)]. At the transition itself, the parabolic formula evaluated just inside the break yields $B_{\text{parab}}(s_{\text{break}}) \simeq 15 \text{ G}$, while the equipartition formula evaluated just outside yields $B_{\text{eq}}(s_{\text{break}} \tan \theta_{\text{open}}) \simeq 0.4 \text{ G}$. The factor- ~ 40 jump is the physical signature of magnetic-to-kinetic conversion at the collimation transition — a known feature of GRMHD jet simulations [33, 35] that occurs over ~ 1 decade in s rather than at a sharp break — and not an inconsistency in the model. The dropped magnetic energy reappears as bulk kinetic energy of the post-collimation jet, leaving P_{BZ} unchanged but redistributed between magnetic and kinetic forms.

Jet-spine equipartition field. Beyond the collimation break, the jet propagates as a free conical flow with cylindrical radius $r_{\perp}(s) = s \tan \theta_{\text{open}}$ measured from the *instantaneous* spin axis (which itself precesses about Galactic \hat{z} on the period T_{prec} ; Sec. 2.3). At any cross-section, equating the Poynting flux P_{BZ} to the magnetic energy density advected at the speed of light through area πr_{\perp}^2 gives [19, 60]

$$B_{\text{jet}}(r_{\perp}) = \left(\frac{8P_{\text{BZ}}}{r_{\perp}^2 c} \right)^{1/2}. \quad (16)$$

We now evaluate particle confinement by calculating the Larmor radius as a function of propagation distance s . In the equipartition regime, the magnetic field scales as s^{-1} . The ratio of the Larmor radius to the local jet radius $r_{\perp} = s \tan \theta_{\text{open}}$ evaluates to

$$\frac{r_L(E_p, s)}{r_{\perp}(s)} = \frac{E_p}{e} \left(\frac{c}{8P_{\text{BZ}}} \right)^{1/2}. \quad (17)$$

This dimensionless ratio remains constant over distance and equals 8.9×10^{-5} for a proton energy of 100 TeV. The Larmor radius is much smaller than the jet width. Inside the bubbles, the ambient field of $5 \mu\text{G}$ yields a Larmor radius of 0.02 pc for the same energy, which is much smaller than the 5 kpc bubble radius. We determine that the magnetic field confines the protons and preserves the injection morphology. With P_{BZ} from Eq. (10), Eq. (16) yields $\sim 140 \mu\text{G}$ at $s = 0.1 \text{ kpc}$ (spine radius $\sim 9 \text{ pc}$) and $\sim 14 \mu\text{G}$ at $s = 1.0 \text{ kpc}$ (spine radius $\sim 90 \text{ pc}$), exceeding the diffuse Galactic-Centre radio field of $\sim 10 \mu\text{G}$ [61, 62] by factors of ~ 14 and ~ 1.4 , respectively. These are *instantaneous* spine values; the field at a fixed Galactic location is reduced by the precession duty cycle $f_{\text{duty}} \simeq \theta_c / (\pi \sin i_{\text{tilt}}) \simeq 0.2$ once the jet has completed $\mathcal{N}_{\text{prec}} \gtrsim$ a few cycles.

Bubble-wall field. At the bubble wall ($s = R_{\text{bub}}$), the asymptotic collimation $\theta_{\text{open}} \simeq 5^\circ$ sets the spine radius $r_{\perp}|_{\text{wall}} = R_{\text{bub}} \tan \theta_{\text{open}} \simeq 0.44 \text{ kpc}$ for $R_{\text{bub}} \simeq 5 \text{ kpc}$ [12, 13]. Inserting into Eq. (16),

$$B_{\text{wall}}^{\text{jet}} \equiv B_{\text{jet}}(r_{\perp}|_{\text{wall}}) \simeq 1.6 \mu\text{G}, \quad (18)$$

the instantaneous spine field. After precession averaging over $\mathcal{N}_{\text{prec}} \simeq 4.7$ cycles, the time-averaged jet contribution is reduced to $\langle B_{\text{wall}}^{\text{jet}} \rangle \sim 0.3 \mu\text{G}$, well below the shock-amplified ambient halo field ($\sim 4 \mu\text{G}$ from $B_{\text{ambient}} \sim 1 \mu\text{G}$ amplified by the forward shock). The total bubble-wall field is therefore dominated by the shock-compressed halo, with the precessing-jet contribution as a sub-dominant correction. The combined value $\sim 5 \mu\text{G}$ is consistent with the observed Fermi-bubble equipartition range $B_{\text{eq}} \approx 4\text{--}8 \mu\text{G}$ [61, 14].

Post-shutoff field decay. After jet shutoff at $t = T_{\text{act}}$, the horizon flux is no longer replenished by accretion. We use a phenomenological exponential decay

$$B_H(t) = \begin{cases} B_H^{(0)} & t \leq T_{\text{act}}, \\ B_H^{(0)} \exp[-(t - T_{\text{act}})/T_{\text{off}}] & t > T_{\text{act}}, \end{cases} \quad (19)$$

with $T_{\text{off}} \simeq 3 \text{ Myr}$, of order the dynamical crossing time of the Sgr A* outflow over the relevant emission region [48, 16].

Table 1: Magnetic field magnitudes at key scales during the active phase of Sgr A*. Spine values use B_{jet} [Eq. (16)] evaluated at the actual spine radius $r_{\perp}(s) = s \tan \theta_{\text{open}}$ for $\theta_{\text{open}} = 5^\circ$.

Location	s along jet	$r_{\perp}(s)$	B
<i>Parabolic regime, $s \leq s_{\text{break}}$</i>			
Horizon	$r_+ = 1.44 r_g$	—	$\sim 2 \times 10^4 \text{ G}$
Jet base	$\sim 10 r_g$	—	$\sim 5 \times 10^3 \text{ G}$
Just inside s_{break}	$\simeq 0.02 \text{ pc}$	—	$\sim 15 \text{ G}$
<i>Equipartition regime, $s > s_{\text{break}}$</i>			
Just outside s_{break}	$\simeq 0.02 \text{ pc}$	$1.7 \times 10^{-3} \text{ pc}$	$\sim 0.7 \text{ G}$
Jet spine (Eq. 16)	0.001 kpc	$\sim 0.09 \text{ pc}$	$\sim 14000 \mu\text{G}$
	0.01 kpc	$\sim 0.9 \text{ pc}$	$\sim 1400 \mu\text{G}$
	0.1 kpc	$\sim 9 \text{ pc}$	$\sim 140 \mu\text{G}$
	1.0 kpc	$\sim 90 \text{ pc}$	$\sim 14 \mu\text{G}$
Bubble wall (jet, instantaneous)	$\sim 5 \text{ kpc}$	$\sim 440 \text{ pc}$	$\sim 2.8 \mu\text{G}$
Bubble wall (jet, time-averaged)	$\sim 5 \text{ kpc}$	$\sim 440 \text{ pc}$	$\sim 0.5 \mu\text{G}$
Bubble wall (jet + shock)	$\sim 5 \text{ kpc}$	$\sim 440 \text{ pc}$	$\sim 5 \mu\text{G}$
Observed FEB (equipartition)	$\sim 5 \text{ kpc}$	$\sim 440 \text{ pc}$	4–8 μG [61]

2.3 Jet geometry: tilt and Lense–Thirring precession

EHT polarimetry and GRMHD modelling constrain the Sgr A* spin axis to a line-of-sight inclination $i \approx 150^\circ$ [16, 17, 18], where i is measured between the Earth–GC direction and the angular-momentum vector. In the Galactic frame, this corresponds to a permanent tilt $i_{\text{tilt}} \simeq 35^\circ$ between the spin axis and the Galactic rotation axis \hat{z} (NGP), the angle relevant for the Lense–Thirring averaging below. We work with $i_{\text{tilt}} = 35^\circ$ as our fiducial value (recalling that EHT constrains the line-of-sight inclination directly, with the geometric translation to Galactic-frame tilt depending on the relative orientation of the Earth–GC line and the Galactic rotation axis), and explore $i_{\text{tilt}} \in [20^\circ, 50^\circ]$.

A misaligned accretion disc undergoes rigid-body Lense–Thirring precession about \hat{z} [63, 64]. For a geometrically thick disc with warp radius r_{warp} , the Lense–Thirring

precession angular frequency is [65, 66]

$$\Omega_{\text{LT}}(r_{\text{warp}}) = \frac{2G^2 M_{\bullet}^2 a_{\star}}{c^3 r_{\text{warp}}^3}. \quad (20)$$

The Bardeen–Petterson alignment radius is fixed by setting the local Lense–Thirring period equal to the jet precession period observed at infinity, $T_{\text{prec}} \equiv 2\pi/\Omega_{\text{LT}}(r_{\text{warp}})$. Inverting Eq. (20),

$$r_{\text{warp}} = \left(\frac{a_{\star} G^2 M_{\bullet}^2 T_{\text{prec}}}{\pi c^3} \right)^{1/3} = r_g \left(\frac{a_{\star} c T_{\text{prec}}}{\pi r_g} \right)^{1/3}. \quad (21)$$

For $a_{\star} = 0.9$, $M_{\bullet} = 4.15 \times 10^6 M_{\odot}$, and our adopted $T_{\text{prec}} = 1.6$ Myr, this yields $r_{\text{warp}} \simeq 9000 r_g \approx 1.8$ mpc. This places the warp well inside the body of the radiatively-inefficient accretion flow [42, 67], where viscous communication times are short enough to support a coherent precessing inner disc–jet system. The mechanism is directly confirmed by the observed 11.24-yr Lense–Thirring jet precession in M87 [68, 69], providing an empirical existence proof for Lense–Thirring precession of misaligned discs around an SMBH. We apply the same physics to Sgr A[∗], with the scaling $T_{\text{prec}} \propto M_{\bullet} (r_{\text{warp}}/r_g)^3$ bringing the M87 11.24-yr period to $\sim 10^6$ yr for the appropriate Sgr A[∗] warp radius. During the active phase the jet completes

$$\mathcal{N}_{\text{prec}} = \frac{T_{\text{act}}}{T_{\text{prec}}} = \frac{7.5 \text{ Myr}}{1.6 \text{ Myr}} \simeq 4.7 \quad (22)$$

full precession cycles. Since $\mathcal{N}_{\text{prec}} \gtrsim$ a few, the time-averaged CR injection is azimuthally uniform at the $1/(2\mathcal{N}_{\text{prec}}) \simeq 10\%$ level, justifying the precession-averaged injection fraction $P(\vartheta)$ derived in Sec. 2.4.

2.4 Precession-averaged CR injection fraction

For $\mathcal{N}_{\text{prec}} \gg 1$ the time-dependent BZ cone is replaced by its azimuthal average. The jet deposits CRs within half-angle $\theta_c = 20^\circ$ of its instantaneous axis (the horizon-scale BZ critical cone, set by the angular structure of the parabolic poloidal field [53, 38]). For a direction at Galactic polar angle ϑ (measured from the North Galactic Pole), the fraction of the precession period during which the upper BZ cone illuminates that direction is

$$P^+(\vartheta) = \frac{1}{\pi} \arccos \left(\frac{\cos \theta_c - \cos \vartheta \cos i_{\text{tilt}}}{\sin \vartheta \sin i_{\text{tilt}}} \right), \quad (23)$$

for $|\cos \theta_c - \cos \vartheta \cos i_{\text{tilt}}| \leq \sin \vartheta \sin i_{\text{tilt}}$; otherwise $P^+ = 0$ or 1. The bipolar injection fraction, including the southern counter-jet contribution $P^-(\vartheta) = P^+(\pi - \vartheta)$, follows from inclusion–exclusion:

$$P(\vartheta) = P^+(\vartheta) + P^-(\vartheta) - P^+(\vartheta) P^-(\vartheta). \quad (24)$$

We evaluate the product $P^+(\vartheta)P^-(\vartheta)$ for the specified geometric parameters. The northern emission band spans polar angles from 15° to 55° . The southern conjugate spans 125° to 165° . These intervals are disjoint. The cross term vanishes identically. The effective injection fraction is the direct sum of the components. For the fiducial parameters, $P(\vartheta)$ is non-zero for $15^\circ < \vartheta < 55^\circ$ (and the conjugate southern range), producing an annular injection enhancement consistent with the observed GCE profile [5, 6].

The estimates in this work depend only on the precession period T_{prec} , the number of completed cycles $\mathcal{N}_{\text{prec}}$, the spin magnitude $|a_{\star}|$, and the tilt magnitude i_{tilt} . They are

independent of: (i) the sign of the spin angular momentum (whether \hat{J}_{BH} points toward the North or South Galactic Pole — a degeneracy not resolved by current EHT data, which favours $i = 150^\circ$ but admits a reflection degeneracy to $i = 30^\circ$ [18]); (ii) the sense of disc rotation about the spin axis (constrained by ALMA polarimetry to be clockwise on the sky as seen from Earth [70], but entering this work only through the precession-averaging); (iii) the sense of Lense–Thirring precession; and (iv) the polarity and handedness of the magnetic field (field-line rotation Ω_F is required by the force-free condition to co-rotate with the BH spin [19], but its sign does not enter any scalar hadronic observable). The averaging in Eq. (23) is manifestly invariant under reversal of the precession sweep direction, and Eq. (24) imposes bipolar symmetry $P(\vartheta) = P(\pi - \vartheta)$, eliminating any preferred north–south asymmetry. The hadronic emissivity is a scalar quantity insensitive to field handedness, and the bulge diffusion is isotropic on the relevant scales. The model therefore corresponds to a parity-symmetric, direction-averaged configuration consistent with the residual directional ambiguities in current EHT and ALMA constraints. Direction-dependent diagnostics — specific north–south GCE asymmetries, jet-base polarisation rotation patterns, synchrotron helicity at the bubble walls, and possible coupling to Galactic-disc rotation — operate at the percent level and are not addressed here.

2.5 Bubble dynamics: Sedov–Taylor expansion

The jet inflates two lobes against the ambient bubble-interior medium with density $\rho_{\text{halo}} = n_{\text{halo}} m_p$, $n_{\text{halo}} \sim 10^{-3} \text{ cm}^{-3}$ — a hot, dilute plasma appropriate for the X-ray-emitting halo gas through which the bubbles expand, consistent with the absence of strong thermal X-ray emission from the bubble interior [71, 72]. Under Sedov–Taylor scaling for a continuous energy injection [73, 74],

$$R_{\text{bub}}(t) \approx \xi \left(\frac{P_{\text{BZ}}}{\rho_{\text{halo}}} \right)^{1/5} t_{\text{eff}}^{3/5}, \quad t_{\text{eff}} = \min(t, T_{\text{act}}), \quad (25)$$

with the dimensionless prefactor $\xi \approx 0.88$ for an adiabatic uniform medium [74]. This gives $R_{\text{bub}}(T_{\text{act}}) \simeq 4 \text{ kpc}$ at the moment of jet shutoff. Subsequent post-shutoff coasting over $\sim 2.6 \text{ Myr}$ [16], combined with contributions from disc winds [48] and possibly TDE-driven outflows [49, 50], brings the present-day Fermi γ -ray bubble extent to $R_{\text{bub}}^{\text{now}} \simeq 5 \text{ kpc}$ [12, 13, 14]. The eROSITA X-ray bubbles extend further ($\sim 7\text{--}14 \text{ kpc}$ [13]), reflecting the leading shock front ahead of the γ -ray contact discontinuity [16].

Precession averaging in bubble dynamics. Although the BZ jet is precessing on timescale $T_{\text{prec}} = 1.6 \text{ Myr}$, the bubble inflation is well-described by the precession-averaged ST estimate above. The bubble sound-crossing time $t_{\text{sc}} \sim R_{\text{bub}}/c_s \sim 1 \text{ Myr}$ is comparable to T_{prec} , while both are several times shorter than T_{act} , so the bubble interior pressure equilibrates over multiple precession cycles during inflation. After $\mathcal{N}_{\text{prec}} \gtrsim$ a few cycles, the bubble inflates as if from a quasi-isotropic source of total power P_{BZ} , with bulk height set by integrated energy rather than by per-direction power. The precession does, however, modify the bubble *shape*: a static jet along \hat{z} (as modelled in [16]) produces a high-aspect-ratio, sharply-peaked biconical bubble with the bulk of energy deposited along the polar axis, whereas a precessing jet at $i_{\text{tilt}} = 35^\circ$ deposits energy preferentially in the band $15^\circ < \vartheta < 55^\circ$ around \hat{z} , producing a wider, more rounded biconical bubble with a flatter top and an over-pressured equatorial waist. This rounded morphology is in qualitative agreement with the observed Fermi/eROSITA bubble shapes, which are

markedly less needle-like than typical AGN-jet inflated cavities (e.g. M87) [75, 76]. The precession-averaging mechanism thus simultaneously explains the spherically-symmetric GCE morphology (Sec. 2.4) and the rounded bubble morphology, both of which are features of the data not naturally produced by a static-jet model. Because the precession period is several times shorter than the bubble inflation timescale ($T_{\text{prec}}/T_{\text{act}} \simeq 1/\mathcal{N}_{\text{prec}} \simeq 0.2$), the bubbles inflate along the precession-averaged jet axis — the Galactic \hat{z} -axis — rather than along the instantaneous spin axis. The observed Fermi/eROSITA bubble axis of symmetry coinciding with Galactic \hat{z} [12, 13, 14] is a direct consequence of $\mathcal{N}_{\text{prec}} \gtrsim$ a few.

2.6 Hadronic gamma-ray luminosity and the GCE budget

The precessing BZ jet proposed in this work injects relativistic CR protons at the GC over the active phase T_{act} . The total CR proton energy injected is $E_{\text{CR}} = \xi_{\text{CR}} P_{\text{BZ}} T_{\text{act}} \simeq 6.2 \times 10^{53}$ erg for $\xi_{\text{CR}} = 0.05$. This value sits in the diffusive-shock-acceleration range $\xi_{\text{CR}} \in [0.01, 0.3]$ established by particle-in-cell and hybrid simulations of supernova-remnant shocks [77, 78, 79, 80]; we adopt the conservative low-end value as our fiducial, recognising that the ~ 3 –14% hadronic floor derived below would scale linearly with ξ_{CR} .

We restrict to the hadronic (CR proton) channel throughout: a leptonic component (e^\pm from BZ pair production or shock acceleration of electrons) is expected to be present but produces a spectrally and morphologically distinct inverse-Compton/bremsstrahlung signature that is not modelled here. Such leptons cool on ~ 1 –10 Myr timescales — comparable to T_{act} — via inverse Compton on the CMB and Galactic-Centre interstellar radiation field and via synchrotron in the bubble magnetic field ($B \sim 5 \mu\text{G}$); their cooled emission therefore traces the bubble interior rather than the diffusively-spread proton population, so the leptonic contribution to the GCE-region emission specifically is expected to be small.

The injected CR protons subsequently interact with ambient gas via $pp \rightarrow \pi^0 \rightarrow \gamma\gamma$, producing the hadronic gamma-ray power [81, 82]

$$L_\gamma = \frac{1}{3} n_{\text{gas}} \sigma_{pp} c E_{\text{CR}}, \quad (26)$$

where $\sigma_{pp} \approx 40 \times 10^{-27} \text{ cm}^2$ and the factor $1/3$ accounts for the fraction of pp inelastic collisions producing π^0 . For the hot, dilute bulge medium with $n_{\text{eff}} \in [0.01, 0.05] \text{ cm}^{-3}$ (Sec. 3.1), the pp cooling time satisfies $t_{pp} \gg T_{\text{act}}$, so CRs are far from hadronic cooling during the active phase.

Other radiative channels are negligible. The CR protons undergo no significant non-hadronic radiative losses during their ~ 10 Myr residence in the bulge. Proton synchrotron radiation is suppressed by a factor $(m_e/m_p)^4 \simeq 10^{-13}$ relative to the electron cooling rate at the same energy and field, giving a cooling time $t_{\text{syn},p} \gtrsim 10^{14}$ yr even in the spine field $B_{\text{jet}} \sim 100 \mu\text{G}$ at $s \sim 0.1$ kpc; proton inverse Compton on the local radiation field is similarly negligible. Adiabatic losses during post-shutoff bubble expansion ($R_{\text{bub}} \rightarrow 1.25 R_{\text{bub}}$ over ~ 2.6 Myr) contribute at most a $\sim 20\%$ correction to the CR energy reaching the present epoch — well within the factor ~ 2 uncertainty on the floor amplitude from the isotropic-cloud approximation (Sec. 3.2). The dominant energy-conversion channel is the $pp \rightarrow \pi^0 \rightarrow \gamma\gamma$ inelastic interaction itself, which converts a fraction $\sim 10^{-3}$ of the injected CR energy to gamma-rays over T_{act} ; this is fully accounted for in Eq. (26) and in the energy-resolved spectrum of Sec. 3.5. CR diffusive escape from the bulge proceeds on

timescale $t_{\text{esc}}(E_p) \simeq R^2/(4D_{\text{bulge}}) \simeq T_{\text{act}}$ for GeV protons, decreasing as $E_p^{-\delta}$ for higher energies under the assumed turbulence spectrum (Sec. 3.5); this energy-dependent escape shapes the high-energy spectrum and is incorporated in the two-zone Green function of Sec. 3.3. Normalising to the observed GCE luminosity $L_{\text{GCE}} \simeq 2.3 \times 10^{37} \text{ erg s}^{-1}$ [5, 4], the *energy-budget upper bound* on the BZ hadronic floor is $L_\gamma/L_{\text{GCE}} \lesssim 5\text{--}30\%$ depending on bulge gas density; the morphology-matched result derived in Sec. 4 tightens this to a non-trivial hadronic floor at the $\sim 3\text{--}14\%$ level.

Between injection and decay, the CRs propagate diffusively through a two-zone medium [83, 84, 85, 86, 87]: the Central Molecular Zone ($r < 200 \text{ pc}$, $D_{\text{CMZ}} = 10^{27} \text{ cm}^2 \text{ s}^{-1}$) and the Galactic bulge ($r \geq 200 \text{ pc}$, $D_{\text{bulge}} = 3 \times 10^{28} \text{ cm}^2 \text{ s}^{-1}$), with the factor- ~ 30 contrast empirically established by HESS observations of the inner $\sim 100 \text{ pc}$ [88] and consistent with theoretical expectations for highly turbulent, magnetised molecular gas [83]. As a first estimate, the characteristic diffusion lengths in the two zones are

$$\lambda_{\text{CMZ}} \equiv \sqrt{4 D_{\text{CMZ}} T_{\text{act}}} \simeq 0.32 \text{ kpc}, \quad (27)$$

$$\lambda_{\text{bulge}} \equiv \sqrt{4 D_{\text{bulge}} T_{\text{act}}} \simeq 1.73 \text{ kpc}, \quad (28)$$

evaluated at $T_{\text{act}} = 7.5 \text{ Myr}$. Already $\lambda_{\text{CMZ}} > 200 \text{ pc}$, so CRs escape the CMZ efficiently into the bulge zone, while λ_{bulge} subtends $\sim 12^\circ$ at $d_\odot = 8.2 \text{ kpc}$ — comparable to the observed GCE extent [5, 6]. This estimate motivates the full two-zone CR transport computation developed in Sec. 3, where the realised hadronic floor (after morphology matching) is derived and subsequently constrained in Sec. 4.

Maximum proton energy. The Larmor radius for a relativistic proton in a uniform field is

$$r_L(E_p) = \frac{E_p}{eB} \simeq 1.08 \times 10^{-6} \text{ pc} \left(\frac{E_p}{1 \text{ PeV}} \right) \left(\frac{B}{1 \text{ G}} \right)^{-1}, \quad (29)$$

and the maximum confinable energy in a magnetised region of size L with shock speed $\beta_{\text{sh}}c$ is the Hillas energy [89]

$$E_p^{\text{max}} = Z e B L \beta_{\text{sh}}. \quad (30)$$

We evaluate Eq. (30) at three relevant sites of the system. (i) Near the black hole horizon, $B \sim 2 \times 10^4 \text{ G}$ within the active jet-launching zone $L \sim 10 r_g$, and $\beta_{\text{sh}} \sim 0.1$ characteristic of the BZ outflow at the fast-magnetosonic surface, giving $E_p^{\text{max}} \simeq 3.7 \text{ EeV}$. (ii) Along the jet spine at $s \simeq 0.1 \text{ kpc}$, the equipartition field is $B \simeq 140 \mu\text{G}$ [Eq. (16)] and the transverse scale is $r_\perp \simeq 9 \text{ pc}$, with $\beta_{\text{sh}} \simeq 0.1$ characteristic of jet shear acceleration [90, 91], yielding $E_p^{\text{max}} \simeq 120 \text{ PeV}$. (iii) At the post-shutoff FEB shock, $B \sim 5 \mu\text{G}$, $L \sim 5 \text{ kpc}$, and $v_{\text{sh}} \simeq 160 \text{ km/s}$ (Sec. 2.5) give $\beta_{\text{sh}} \simeq 5 \times 10^{-4}$ and $E_p^{\text{max}} \simeq 12 \text{ PeV}$. Sites (i), (ii), and (iii) all comfortably accommodate our adopted spectral cutoff $E_p^{\text{max}} = 100 \text{ TeV}$ by at least three orders of magnitude, so cosmic-ray acceleration is not energy-limited within the fiducial model. The BZ-jet model acceleration is consistent with proton injection up to $\gtrsim 100 \text{ TeV}$ at the jet base and spine, with subsequent diffusion into the bulge populating the GCE region at energies $E_p \lesssim E_p^{\text{max}}$.

Fiducial parameters. The full set of fiducial parameters and derived quantities is collected in Table 2 for reference.

Table 2: Fiducial model parameters and derived quantities.

Quantity	Symbol	Fiducial value
<i>Black hole and accretion</i>		
BH mass	M_{\bullet}	$4.15 \times 10^6 M_{\odot}$
BH spin	a_{\star}	0.9
Eddington fraction	\dot{m}	1×10^{-5}
BZ efficiency	η_{BZ}	$\simeq 0.9$
BZ jet power	P_{BZ}	$5.2 \times 10^{40} \text{ erg s}^{-1}$
<i>Magnetic field</i>		
Horizon field (active)	$B_H^{(0)}$	$2 \times 10^4 \text{ G}$
Bubble-wall field	B_{wall}	$\sim 5 \mu\text{G}$
Collimation break	s_{break}	$\sim 0.02 \text{ pc}$
Asymptotic opening	θ_{open}	5°
<i>Geometry and timing</i>		
Spin-axis tilt	i_{tilt}	35°
BZ cone half-angle	θ_c	20°
Active duration	T_{act}	7.5 Myr
Time since shutoff	T_{off}	$\sim 2.6 \text{ Myr}$
Precession period	T_{prec}	1.6 Myr
Number of LT cycles	$\mathcal{N}_{\text{prec}}$	$\simeq 4.7$
Warp radius	r_{warp}	$\simeq 9000 r_g$
<i>Cosmic-ray transport and gamma-rays</i>		
CR injection efficiency	ξ_{CR}	$\simeq 0.05$
D (CMZ)	D_{CMZ}	$10^{27} \text{ cm}^2 \text{ s}^{-1}$
D (bulge)	D_{bulge}	$3 \times 10^{28} \text{ cm}^2 \text{ s}^{-1}$
Diffusion length (bulge)	λ_{bulge}	1.73 kpc ($\sim 12^\circ$)
Diffusion length (CMZ)	λ_{CMZ}	0.32 kpc ($\sim 2.2^\circ$)
CMZ outer boundary	R_b	200 pc
Total jet energy	E_{jet}	$\simeq 1.2 \times 10^{55} \text{ erg}$
Total CR energy	E_{CR}	$\simeq 6.2 \times 10^{53} \text{ erg}$
Bubble radius (today)	R_{bub}	$\simeq 5 \text{ kpc}$
GCE hadronic floor (energy)	$L_{\gamma}/L_{\text{GCE}}$	$\lesssim 5\text{--}30\%$
GCE hadronic floor (morph.)	$L_{\gamma}/L_{\text{GCE}}$	$\sim 5\text{--}10\%$

3. Derivation of the Hadronic Gamma-Ray Surface Brightness

In this section we derive the gamma-ray surface brightness produced by hadronic CR proton interactions in the inner Galaxy, starting from the volume emissivity (Sec. 3.1) and progressing through the isotropic CR cloud assumption (Sec. 3.2), the two-zone diffusion Green function (Sec. 3.3), the line-of-sight integral (Sec. 3.4), the energy-resolved spectrum (Sec. 3.5), and the caveats of the spatial-spectral factorisation (Sec. 3.6). The precession-averaged angular factor $P(\vartheta)$ derived in Sec. 2.4 of the model description enters the formal multipole analysis of Appendix B; we show in Sec. 3.2 below that diffusive smearing washes it out at GCE-relevant radii, so the fiducial calculation adopts a fully isotropic CR cloud. Throughout, θ denotes the angular distance of an observation direction from the Galactic Centre on the sky, while ϑ denotes the polar angle measured from the Galactic rotation axis (which coincides with the precession-averaged spin axis); the two coincide only for $\ell = 0$ and small θ .

3.1 Volume emissivity from $pp \rightarrow \pi^0 \rightarrow \gamma\gamma$

For cosmic-ray protons interacting with diffuse interstellar gas, the dominant gamma-ray production channel above $E_\gamma \simeq 0.3$ GeV is inelastic proton-proton scattering producing neutral pions which decay to photon pairs [92, 93, 81, 94]:

$$p + p \rightarrow X + \pi^0, \quad \pi^0 \rightarrow \gamma + \gamma. \quad (31)$$

For a CR proton population with differential number density $n_{\text{CR}}(E_p, \mathbf{x})$ (units $\text{cm}^{-3} \text{GeV}^{-1}$) traversing a target gas of density $n_{\text{gas}}(\mathbf{x})$, the differential photon volume emissivity at energy E_γ is [81, 94]

$$\varepsilon(E_\gamma, \mathbf{x}) = c n_{\text{gas}}(\mathbf{x}) \int_{E_{\text{th}}}^{\infty} \frac{d\sigma_{pp}(E_p, E_\gamma)}{dE_\gamma} n_{\text{CR}}(E_p, \mathbf{x}) dE_p, \quad (32)$$

in units of $\text{ph cm}^{-3} \text{s}^{-1} \text{GeV}^{-1}$, where c is the speed of light and $E_{\text{th}} \simeq 1.22$ GeV is the proton kinetic threshold for π^0 production. We use the Kafexhiu et al. [94] parametrisation of $d\sigma_{pp}/dE_\gamma$, which is valid from threshold to PeV energies and reproduces accelerator data to better than 20%.

For the present model, energy losses are negligible during the active phase ($t_{pp} \gg T_{\text{act}}$, Sec. 2.6). The diffusion length $\lambda(E_p) \propto E_p^{\delta/2}$ varies by a factor of ~ 3 across the GeV–TeV proton energies that dominate the GCE band; we capture this energy dependence in the in-bulge spectrum $q(E_p)$ via the leaky-box treatment of Sec. 3.5, while keeping the spatial Green function of Sec. 3.3 fixed at the GeV-scale diffusion coefficient. This factorised treatment is the standard methodology in inner-Galaxy hadronic gamma-ray analyses [95, 96, 97]; the leading correction from energy-dependent spatial spreading is bounded at the $\sim 30\%$ level and is discussed in Sec. 3.6. The CR proton spectrum therefore retains its shape $q(E_p)$ at every point in the bulge, and the differential density factorises:

$$n_{\text{CR}}(E_p, \mathbf{x}) = n_{\text{CR}}(\mathbf{x}) q(E_p), \quad \int q(E_p) dE_p = 1, \quad (33)$$

where $n_{\text{CR}}(\mathbf{x})$ has units cm^{-3} (energy-integrated number density), $q(E_p)$ has units GeV^{-1} (position-independent normalised energy shape from the BZ injection, Sec. 3.5), and the

diffusion Green function of Sec. 3.3 provides $n_{\text{CR}}(\mathbf{x})$. The total CR energy injected during T_{act} is related to the spatial integral by

$$E_{\text{CR}} = \bar{E}_p \int 4\pi r^2 n_{\text{CR}}(r) dr, \quad \bar{E}_p \equiv \int E_p q(E_p) dE_p, \quad (34)$$

where \bar{E}_p is the mean proton energy of the injection spectrum; for our fiducial $\alpha = 2.4$, $E_p^{\text{min}} = 1 \text{ GeV}$, $E_p^{\text{max}} = 100 \text{ TeV}$, this gives $\bar{E}_p \simeq 2.7 \text{ GeV}$.²

Substituting Eq. (33) into Eq. (32), the emissivity separates into independent spatial and energy factors:

$$\varepsilon(E_\gamma, \mathbf{x}) = \underbrace{n_{\text{gas}}(\mathbf{x}) n_{\text{CR}}(\mathbf{x})}_{\text{spatial}} \times c \underbrace{\int \frac{d\sigma_{pp}}{dE_\gamma} q(E_p) dE_p}_{\text{energy (per CR)}}. \quad (35)$$

For the dilute, hot bulge medium the gas density is approximately uniform on the scales of interest. We consider

$$n_{\text{gas}}(\mathbf{x}) \approx n_{\text{eff}} \simeq 0.03 \text{ cm}^{-3} \quad (n_{\text{eff}} \in [0.01, 0.05] \text{ cm}^{-3}), \quad (36)$$

the central value $n_{\text{eff}} = 0.03 \text{ cm}^{-3}$ corresponding to the inner Milky Way hot ($T \sim 10^{6-7} \text{ K}$) ionised halo measured in OVII/OVIII X-ray absorption toward background AGN [47] and emission mapping [98, 99, 13]. The band spans the conservative inner-bulge range, with the lower bound 0.01 cm^{-3} appropriate to the depleted Fermi-bubble cavity interior [71, 72] and the upper bound 0.05 cm^{-3} matching the Miller–Bregman β -model central density $n_e^{(0)} = 0.046 \text{ cm}^{-3}$. The spatial structure of ε is therefore controlled by $n_{\text{CR}}(\mathbf{x})$ alone in this fiducial calculation; the more realistic decomposition $n_{\text{gas}}(\mathbf{x}) = n_{\text{bar}}(\mathbf{x}) + n_{\text{halo}}$ including the triaxial bar is developed in Sec. 5, where it gives rise to the longitudinal asymmetry of the GCE.

3.2 Isotropic CR cloud approximation

The precession-averaged source pattern $P(\vartheta)$ derived in Sec. 2.4 is non-zero only in the polar band $15^\circ \leq \vartheta \leq 55^\circ$ and its southern conjugate, with $P(\vartheta) = 0$ both near the Galactic poles ($\vartheta < 15^\circ$) and near the Galactic plane ($\vartheta > 55^\circ$). Naively this would predict an annular morphology for the GCE, in tension with the observed approximately spherical profile. Diffusion, however, washes out this angular pattern between the deposition cutoff $r_{\text{dep}} = 100 \text{ pc}$, defined as the radius beyond which diffusive isotropisation exceeds the source cone half-width (see Eq. 39 below), and the GCE-relevant radii $r \sim 1\text{--}2 \text{ kpc}$.

The angular diffusion smearing scale is set by the characteristic angular spread of CRs at radius r after diffusion time t ,

$$\sigma_\vartheta(r, t) \simeq \frac{\sqrt{4D(t)t}}{r} = \frac{\lambda(t)}{r}, \quad (37)$$

²The injection spectrum is bounded at $E_p^{\text{min}} = 1 \text{ GeV}$, just above the $pp \rightarrow \pi^0$ threshold ($E_{\text{th}} \simeq 1.22 \text{ GeV}$) so that every modelled proton can contribute to the γ -ray signal, and at $E_p^{\text{max}} = 100 \text{ TeV}$, two orders of magnitude below the Hillas ceiling $eBr_g \sim 10 \text{ PeV}$ for fiducial jet parameters $B \sim 10^4 \text{ G}$ and $R_{\text{acc}} \sim r_g$. The morphological and spectral results in the GCE band are insensitive to E_p^{max} above $\sim 1 \text{ TeV}$, since the protons producing $\sim 100 \text{ GeV}$ photons have $E_p \sim 1 \text{ TeV}$.

where $\lambda(t) = \sqrt{4Dt}$ is the diffusion length. At GCE-relevant radii $r \sim 1$ kpc with our fiducial $D_{\text{bulge}} = 3 \times 10^{28} \text{ cm}^2 \text{ s}^{-1}$ and active time $T_{\text{act}} = 7.5 \text{ Myr}$,

$$\sigma_{\vartheta}(1 \text{ kpc}, T_{\text{act}}) \simeq \frac{1.73 \text{ kpc}}{1 \text{ kpc}} \simeq 1.7 \text{ rad} \simeq 100^\circ, \quad (38)$$

much larger than the source band half-width $\theta_c \equiv (55^\circ - 15^\circ)/2 = 20^\circ$. The CR cloud is therefore effectively isotropic at GCE-relevant radii: each angular structure in the source is averaged over a diffusion patch comparable in size to the full 4π sphere.

Setting $\sigma_{\vartheta}(r, T_{\text{act}}) \gtrsim \theta_c$ gives

$$r \lesssim \frac{\lambda_{\text{bulge}}}{\theta_c} \simeq 290 \text{ pc} \quad (39)$$

as the radius below which the isotropic ansatz is not strictly justified. We adopt the more conservative $r_{\text{dep}} = 100 \text{ pc}$ as the deposition cutoff, ensuring diffusive smearing exceeds the source pattern width by a factor of at least five at every contributing radius [95].

We accordingly approximate the CR density as spherically symmetric,

$$n_{\text{CR}}(\mathbf{x}) \approx n_{\text{CR}}(r), \quad (40)$$

with the angular pattern $P(\vartheta)$ fully averaged out by diffusive isotropisation. The radial profile $n_{\text{CR}}(r)$ is then governed by the spherically-symmetric diffusion problem with point-source injection, solved in Sec. 3.3 below. A formal multipole expansion of the diffusion equation, decomposing the source $P(\vartheta)$ into Legendre coefficients and tracking each moment $\ell \geq 1$ separately, is given in Appendix B. The leading higher moments decay as $\exp[-\ell(\ell+1)Dt/r^2]$ relative to the monopole, so that for $r \ll \lambda_{\text{bulge}}$ all $\ell \geq 1$ contributions are suppressed by factors $\gtrsim 10^2$. We retain only the monopole in the main text.

This approximation breaks down in two limits not covered by our fiducial case. For slow precession ($\mathcal{N}_{\text{prec}} \lesssim 1$), the source pattern depends on the orientation of the jet at specific times rather than on the azimuthally-averaged $P(\vartheta)$, introducing an additional ϕ -dependence; for our fiducial $\mathcal{N}_{\text{prec}} \simeq 4.7$ this is bounded by $\sim 1/(2\mathcal{N}_{\text{prec}}) \simeq 10\%$. For anisotropic diffusion (e.g. field-aligned transport along the bubble walls), CRs propagate preferentially along magnetic-field directions, distorting the angular pattern as they spread. Both effects produce percent-level corrections at most and are discussed further in Sec. 6.

3.3 Two-zone CR diffusion Green function

We assume CRs are accelerated within the BZ-launched jet column on scales $r \lesssim r_{\text{dep}} = 100 \text{ pc}$, between the launching region near the BH and the parabolic-to-conical transition near the Bondi radius. On these scales acceleration proceeds by reconnection in the BZ-launched flow, internal shocks, and shear acceleration along the jet column [100, 90]. The angular imprint of the source is washed out by diffusion at GCE radii (Sec. 3.2), so the CR density entering the LOS integral depends only on the Galactocentric distance r ; the radial spread is governed by the diffusion equation derived in this subsection. CRs escape laterally into the bulge ISM and diffuse outward through the two-zone medium described below.

Because the deposition scale satisfies $r_{\text{dep}} \ll \lambda_{\text{bulge}} = 1.73 \text{ kpc}$, the source is effectively pointlike for radial transport on GCE-relevant scales. We therefore model it as a delta function at the GC; the radial Green function $n_{\text{CR}}(r)$ derived in this subsection captures

the diffusive spread. We do not model deposition at the jet termination shock or volume-filling deposition in an inflated bubble cocoon; those scenarios are appropriate for the Fermi/eROSITA bubble morphology [16, 48, 39] but predict gamma-ray emission extended over $\sim 50^\circ$ rather than the centrally-concentrated $\sim 12^\circ$ GCE we target here.

Diffusion equation. CR transport in the bulge is governed by

$$\frac{\partial n_{\text{CR}}}{\partial t} = \nabla \cdot [D(\mathbf{x}) \nabla n_{\text{CR}}] + Q(\mathbf{x}, t), \quad (41)$$

with energy losses neglected because the inelastic pp cooling time satisfies $t_{pp} \gg T_{\text{act}}$ for $n_{\text{eff}} \lesssim 10^{-2} \text{ cm}^{-3}$ (Sec. 2.6). For the radial calculation we take

$$Q(\mathbf{x}, t) = Q_0 \delta^3(\mathbf{x}) \Theta(t) \Theta(T_{\text{act}} - t), \quad (42)$$

where Q_0 is the constant total CR injection rate (particles per second), to be fixed below by the energy-budget constraint. The energy-resolved injection rate is recovered by multiplication with the normalised energy shape $q(E_p)$ from Eq. (33): $dN/(dE_p dt) = Q_0 q(E_p)$, where the un-normalised spectrum $Q(E_p)$ specified in Sec. 3.5 satisfies $Q(E_p) = Q_0 q(E_p)$ (units $\text{s}^{-1} \text{ GeV}^{-1}$).

For a continuous isotropic point source active over $t \in [0, T]$, time-integrating the three-dimensional Gaussian Green function yields the steady-state CR density at distance r from the source [101, 102]:

$$n_{\text{CR}}(r) = \frac{Q_0}{4\pi D r} \text{erfc}\left(\frac{r}{\lambda}\right), \quad \lambda \equiv \sqrt{4DT}, \quad (43)$$

in units of cm^{-3} . Although our jet has shut off ($\tau_{\text{off}} \simeq 2.6 \text{ Myr}$), this duration is short compared to $T_{\text{act}} = 7.5 \text{ Myr}$, and the post-shutoff free-streaming diffusion contributes only an $\sim 30\%$ correction to the active-phase Green function. We adopt the active-phase form throughout, absorbing the post-shutoff correction into the $\sim 20\%$ adiabatic loss already accounted for in Sec. 2.6.

Two-zone structure. The model contains three nested radial scales controlling cosmic-ray transport: the deposition cutoff $r_{\text{dep}} = 100 \text{ pc}$ (set by the isotropisation argument of Sec. 3.2 and excluded from the LOS integral), the CMZ-bulge boundary $R_b = 200 \text{ pc}$ (set by the molecular gas distribution, where the diffusion coefficient transitions), and the bulge confinement radius $R_{\text{bulge}} = 2 \text{ kpc}$ (which sets the leaky-box escape time in Sec. 3.5). Each of these radii is anchored by an independent physical argument and is not a fitting parameter of the model. The bulge medium is not homogeneous: the dense, magnetised Central Molecular Zone ($r_{\text{dep}} \leq r \leq R_b$) exhibits suppressed diffusion $D_{\text{CMZ}} = 10^{27} \text{ cm}^2 \text{ s}^{-1}$, while the surrounding bulge has $D_{\text{bulge}} = 3 \times 10^{28} \text{ cm}^2 \text{ s}^{-1}$ [83, 84, 85, 86, 87]. The boundary $R_b = 200 \text{ pc}$ is set by HESS observations of the inner $\sim 100\text{--}200 \text{ pc}$ [88]; varying R_b within the literature range $100\text{--}300 \text{ pc}$ changes the morphology fit by $\lesssim 5\%$. We work with the piecewise-constant prescription

$$D(r) = \begin{cases} D_{\text{CMZ}} & r < R_b, \\ D_{\text{bulge}} & r \geq R_b, \end{cases} \quad (44)$$

with corresponding diffusion lengths (28) at $T_{\text{act}} = 7.5 \text{ Myr}$. Note that λ_{bulge} subtends $\sim 12^\circ$ at d_\odot , comparable to the observed GCE extent [5, 6].

Continuity-matched solution. Equation (43) does not satisfy continuity of both density *and* flux at $r = R_b$ if D jumps discontinuously. We therefore solve Eq. (41) separately in each zone and impose $n_{\text{CR}}^{\text{in}}(R_b) = n_{\text{CR}}^{\text{out}}(R_b)$ and $D_{\text{CMZ}} \partial_r n_{\text{CR}}^{\text{in}}|_{R_b} = D_{\text{bulge}} \partial_r n_{\text{CR}}^{\text{out}}|_{R_b}$. The matched solution is

$$n_{\text{CR}}(r) = \begin{cases} \frac{Q_0}{4\pi D_{\text{CMZ}} r} \operatorname{erfc}\left(\frac{r}{\lambda_{\text{CMZ}}}\right) + \frac{b_2}{r}, & r < R_b, \\ \frac{b_1 Q_0}{4\pi D_{\text{bulge}} r} \operatorname{erfc}\left(\frac{r}{\lambda_{\text{bulge}}}\right), & r \geq R_b, \end{cases} \quad (45)$$

with the matching constants

$$b_1 = \frac{2e^{-R_b^2/\lambda_{\text{CMZ}}^2}}{\sqrt{\pi}\lambda_{\text{CMZ}}} \left[\frac{2e^{-R_b^2/\lambda_{\text{bulge}}^2}}{\sqrt{\pi}\lambda_{\text{bulge}}} + \frac{\operatorname{erfc}(R_b/\lambda_{\text{bulge}})}{R_b} \left(1 - \frac{D_{\text{CMZ}}}{D_{\text{bulge}}}\right) \right]^{-1}, \quad (46)$$

$$b_2 = \frac{Q_0}{4\pi} \left[\frac{b_1 \operatorname{erfc}(R_b/\lambda_{\text{bulge}})}{D_{\text{bulge}}} - \frac{\operatorname{erfc}(R_b/\lambda_{\text{CMZ}})}{D_{\text{CMZ}}} \right]. \quad (47)$$

The $(1 - D_{\text{CMZ}}/D_{\text{bulge}})$ factor in b_1 encodes the diffusion-coefficient discontinuity at the CMZ–bulge boundary, required by flux continuity at $r = R_b$. For our fiducial parameters $b_1 \simeq 0.49$. The slower diffusion in the inner zone enhances the CR density at $r < R_b$ relative to a naive single-zone bulge-only solution: at $r = R_b$, the two-zone density is enhanced by a factor ~ 30 due to the $30\times$ slower diffusion coefficient. The matching constant $b_1 \simeq 0.49$ encodes the suppression of the bulge-zone CR density relative to a naive single-zone bulge solution, reflecting partial confinement of CRs in the slower-diffusion CMZ zone.

Factorisation of the surface brightness. The decomposition of the observed surface brightness into a spatial column density $\mathcal{L}(\theta)$ and an energy prefactor $f_{\text{shape}}(E_\gamma)$ in Eq. (53) treats the spatial profile as energy-independent, evaluated at the GeV-scale diffusion coefficient that characterises the bulk of the CR energy budget. Energy-dependent escape of higher-energy protons is incorporated into f_{shape} via the leaky-box treatment of Sec. 3.5. This factorised approach is the standard methodology in inner-Galaxy hadronic gamma-ray analyses [95], and rests on the leaky-box framework of galactic CR propagation [96, 97]. The leading correction from energy-dependent spatial spreading, bounded by the factor-of-3 variation in $\lambda(E_p)$ across the GCE-band proton energies, is discussed in Sec. 3.6.

The normalisation Q_0 is fixed by demanding that the total CR energy injected during the active phase equal $E_{\text{CR}} = \xi_{\text{CR}} P_{\text{BZ}} T_{\text{act}}$, with the isotropic CR density of Eq. (45) satisfying

$$E_{\text{CR}} = \bar{E}_p \int_0^\infty 4\pi r^2 n_{\text{CR}}(r) dr. \quad (48)$$

For our fiducial parameters this gives Q_0 such that $E_{\text{CR}} \simeq 6.2 \times 10^{53}$ erg at $\xi_{\text{CR}} = 0.05$ (see Table 2).

3.4 Line-of-sight integral and surface brightness

The signal observed at Earth in a given sky direction is the sum of the photons emitted by every volume element along that line of sight. Because the π^0 -decay photons are emitted isotropically, only a fraction $1/(4\pi)$ of the volume emissivity reaches each steradian of

sky. The observed photon flux per steradian along a line of sight at sky position (ℓ, b) is therefore

$$I(\theta, E_\gamma) \equiv \frac{dN}{dE_\gamma dt d\Omega}(\ell, b) = \frac{1}{4\pi} \int_0^{S_{\max}} \varepsilon(E_\gamma, \mathbf{x}(s; \ell, b)) ds, \quad (49)$$

in units of $\text{ph cm}^{-2} \text{s}^{-1} \text{GeV}^{-1} \text{sr}^{-1}$, where s is the line-of-sight distance from Earth and $S_{\max} = 14$ kpc extends just beyond the GC on the far side of the Galaxy. The truncation is exact at the level of the morphology fit: the BZ-injected CR density is negligible at distances larger than a few diffusion lengths $\lambda_{\text{bulge}} \simeq 1.73$ kpc from the GC. Galactic-disc gamma-ray emission is not included in the calculation because the Di Mauro 2021 GCE analysis [5] to which we compare has already masked the disc ($|b| < 2^\circ$) and subtracted the diffuse inverse-Compton, bremsstrahlung, and point-source templates; what remains is the residual GCE.

For a point at distance s along a line of sight at Galactic longitude $\ell = 0$ and latitude b , the Galactocentric position has cylindrical components ρ_{GC} (perpendicular to the spin axis) and z_{GC} (parallel to it):

$$\rho_{\text{GC}}(s, b) = |d_\odot - s \cos b|, \quad z_{\text{GC}}(s, b) = s \sin b. \quad (50)$$

The Galactocentric radius and the polar angle from the Galactic rotation axis are

$$r(s, b) = \sqrt{\rho_{\text{GC}}^2 + z_{\text{GC}}^2}, \quad (51)$$

$$\vartheta(s, b) = \arctan(\rho_{\text{GC}}/z_{\text{GC}}) \in [0, \pi], \quad (52)$$

defined so that $\vartheta = 0$ corresponds to the NGP and $\vartheta = \pi$ to the SGP, with $\vartheta = \pi/2$ in the Galactic plane. The radial coordinate r is the only Galactocentric input required by the spherically-symmetric CR density $n_{\text{CR}}(r)$ from Sec. 3.3; the polar angle ϑ is retained for the multipole analysis of Appendix B and for the triaxial gas calculation of Sec. 5, but does not enter the fiducial isotropic-cloud LOS integral developed below. Because the CR distribution and the gas density are azimuthally symmetric about the Galactic rotation axis, the surface brightness depends only on the angular distance θ from the GC on the sky; for $\ell = 0$, $\theta = |b|$, and Eqs. (51)–(52) apply directly.

Substituting Eq. (35) into Eq. (49) and using the isotropic CR cloud approximation of Sec. 3.2, the surface brightness separates into an energy prefactor and a purely geometric line-of-sight integral:

$$I(\theta, E_\gamma) = \frac{1}{4\pi} f_{\text{shape}}(E_\gamma) \mathcal{L}(\theta), \quad (53)$$

where the geometric LOS integral is

$$\mathcal{L}(\theta) \equiv \int_0^{S_{\max}} n_{\text{CR}}(r(s, \theta)) \Theta(r(s, \theta) - r_{\text{dep}}) ds, \quad (54)$$

in units of cm^{-2} (CR column number density), with the Heaviside cutoff $\Theta(r - r_{\text{dep}})$ excluding the inner $r < r_{\text{dep}} = 100$ pc zone in which the isotropic ansatz is not strictly justified (Sec. 3.2). The energy prefactor $f_{\text{shape}}(E_\gamma)$ is defined as

$$f_{\text{shape}}(E_\gamma) = n_{\text{eff}} c \int_{E_{\text{th}}(E_\gamma)}^\infty \frac{d\sigma_{pp}}{dE_\gamma}(E_p, E_\gamma) q(E_p) dE_p, \quad (55)$$

in units of $\text{s}^{-1} \text{GeV}^{-1}$ (spectrum-averaged emissivity per CR proton, with the n_{eff} factor absorbed). $E_{\text{th}}(E_\gamma)$ is the kinematic threshold for π^0 production. The factorisation

Eq. (53) gives $I(\theta, E_\gamma)$ in the correct surface brightness units $\text{cm}^{-2} \text{s}^{-1} \text{GeV}^{-1} \text{sr}^{-1}$, with $\mathcal{L}(\theta)$ depending only on the spatial ingredients and $f_{\text{shape}}(E_\gamma)$ depending only on the spectrum.

We calculate the optical depth to photon-photon pair production to verify the assumption of negligible radiative attenuation. Gamma rays interact with the interstellar radiation field. For a 100 GeV gamma ray, the threshold condition requires target photons with energies near 2.6 eV. We use an average target photon density $n_{\text{ISRF}} \sim 1 \text{ cm}^{-3}$ and a cross section $\sigma_{\gamma\gamma} \simeq 1.2 \times 10^{-25} \text{ cm}^2$. The optical depth over the distance to the Galactic Centre evaluates to

$$\tau_{\gamma\gamma} = \int_0^{d_\odot} n_{\text{ISRF}} \sigma_{\gamma\gamma} ds \simeq 0.003. \quad (56)$$

Because the optical depth satisfies $\tau_{\gamma\gamma} \ll 1$, the interstellar medium is optically thin and the collisionless geometrical line-of-sight integral can be used.

3.5 Energy-resolved spectrum: leaky-box treatment

The in-bulge CR spectrum is shaped by the competition between continuous injection over T_{act} and energy-dependent diffusive escape from the bulge. Following the leaky-box treatment of cosmic-ray escape applied to inner-Galaxy hadronic gamma-ray emission (author?) [95], we define the effective in-bulge residence time as

$$\tau_{\text{eff}}(E_p) = \min \left[T_{\text{act}}, \frac{R_{\text{bulge}}^2}{6 D_0 (E_p/E_0)^\delta} \right] \quad (57)$$

with $R_{\text{bulge}} = 2 \text{ kpc}$, $D_0 = 3 \times 10^{28} \text{ cm}^2 \text{ s}^{-1}$, $E_0 = 1 \text{ GeV}$, and $\delta = 0.5$ for Kraichnan turbulence in the inner Galaxy [87]. The in-bulge differential CR number distribution is

$$N(E_p) \propto Q(E_p) \tau_{\text{eff}}(E_p), \quad (58)$$

with $Q(E_p) = Q_0 E_p^{-\alpha} \exp(-E_p/E_p^{\text{max}})$ the injection rate per unit E_p , $\alpha = 2.4$ the diffusive shock acceleration slope, and $E_p^{\text{max}} = 100 \text{ TeV}$ the Hillas-criterion proton cutoff. This produces a spectral break at

$$E_p^* \equiv E_0 \left(\frac{R_{\text{bulge}}^2}{6 D_0 T_{\text{act}}} \right)^{1/\delta} \simeq 0.8 \text{ GeV}, \quad (59)$$

above which $\tau_{\text{eff}}(E_p) < T_{\text{act}}$ and CRs leak out of the bulge before the active phase ends. Below E_p^* , $\tau_{\text{eff}} = T_{\text{act}}$ and the spectrum keeps the injection slope $\alpha = 2.4$; above E_p^* , $\tau_{\text{eff}} \propto E_p^{-\delta}$ and the in-bulge spectrum steepens to $\alpha + \delta = 2.9$. The normalised shape $q(E_p)$ entering Eq. (33) is

$$q(E_p) = \frac{N(E_p)}{\int_{E_p^{\text{min}}}^{\infty} N(E'_p) dE'_p}. \quad (60)$$

3.6 Caveats of the spatial-spectral factorisation

The factorisation $I(\theta, E_\gamma) = \mathcal{L}(\theta) f_{\text{shape}}(E_\gamma)/(4\pi)$ used in Eq. (53) treats the LOS column density $\mathcal{L}(\theta)$ as evaluated at the GeV-scale diffusion coefficient, while including the energy-dependence of CR escape only in the spectral factor f_{shape} via the leaky-box residence time $\tau_{\text{eff}}(E_p)$ of Eq. (57). A fully self-consistent calculation would evaluate $\mathcal{L}(\theta, E_p)$ at each

proton energy, since $\lambda_{\text{bulge}}(E_p) = \sqrt{4D_0 (E_p/E_0)^\delta T_{\text{act}}}$ grows from 1.7 kpc at $E_p = 1$ GeV to 5.5 kpc at $E_p = 100$ GeV — a factor of ~ 3 across the GCE-band parents.

This factorised treatment is the standard approximation in inner-Galaxy hadronic gamma-ray studies [95], and rests on the textbook leaky-box framework of galactic CR propagation [96, 97]. Its accuracy has been benchmarked against fully energy-resolved transport calculations and shown to capture the leading morphology at the $\sim 30\%$ level for source geometries similar to ours. We adopt it here for analytic tractability and to enable direct comparison with the published GCE template fits. A fully energy-resolved treatment in which both $D_{\text{CMZ}}(E_p)$ and $D_{\text{bulge}}(E_p)$ vary with E_p — using e.g. the Green-function methodology of [101] applied to the two-zone medium — is deferred to future work.

4. Galactic Spectrum and Brightness

Using the framework developed in Sec. 3, we compute the hadronic GCE surface brightness profile and spectrum produced by the precessing BZ jet model at fiducial parameters. Figures 3 and 4 compare the calculations against the Di Mauro 2021 measurements [5] for the spectrum integrated over $\theta < 10^\circ$ and the surface brightness profile in the 1–10 GeV band, respectively.

The computed hadronic spectrum is strongly spin-dependent through the BZ efficiency $\eta_{\text{BZ}}(a_\star)$. At the EHT-favoured high spin $a_\star = 0.9$ and fiducial $n_{\text{eff}} = 0.03 \text{ cm}^{-3}$, the ROI-averaged amplitude reaches $\sim 2.7 \times 10^{-4} \text{ MeV cm}^{-2} \text{ s}^{-1} \text{ sr}^{-1}$ near the π^0 -decay peak at $E_\gamma \simeq 0.5 \text{ GeV}$, saturating the Di Mauro detections and approaching the 95% upper limits in the upper half of the n_{eff} band. Near the GCE spectral peak ($E_\gamma \simeq 1.8 \text{ GeV}$) the contribution is $\sim 25\text{--}45\%$ of the data, falling to $\sim 25\%$ at $E_\gamma = 10 \text{ GeV}$ and rising again to $\sim 30\text{--}70\%$ above $E_\gamma \simeq 30 \text{ GeV}$ where the GCE log-parabola steepens. This places the fiducial high-spin model in mild tension with the sub-GeV upper limits at the upper end of the n_{eff} band, favouring either n_{eff} at the lower end (the depleted bubble-cavity gas of [71, 72]) or a CR injection efficiency ξ_{CR} slightly below the Diffusive Shock Acceleration (DSA) low-end value. The hadronic tail above $\sim 100 \text{ GeV}$ crosses the GCE upper limits — testable with CTA and HAWC.

The angular profile in the 1–10 GeV band at the EHT-favoured $a_\star = 0.9$ is substantially flatter than the cuspy NFW² best-fit ($\gamma = 1.27$): at $\theta = 0.5^\circ$ the model contributes $\sim 6\%$ of the GCE, rising monotonically to $\sim 14\%$ at $\theta = 9.5^\circ$ and falling to $\sim 10\%$ at the outer edge of the GCE ROI ($\theta = 14^\circ$). Two physical features drive this shallowness: the bulge diffusion length $\lambda_{\text{bulge}} = 1.73 \text{ kpc}$ smears the central injection over $\sim 12^\circ$, and the precession-averaged isotropic injection deposits CRs preferentially in the diffusion-broadened sphere rather than at the GC cusp. Both effects produce a centrally-suppressed hadronic contribution relative to the steep NFW² cusp. At lower spin the brightness floor scales with $\eta_{\text{BZ}}(a_\star)$ and drops to $\sim 3\%$ at $a_\star = 0.75$ and below $\sim 1\%$ at $a_\star \leq 0.5$.

We quantify these visual conclusions through χ^2 fits of the expected hadronic surface brightness profile to the Di Mauro 2021 latitude profile [5], which contains 15 angular bins spanning $\theta \in [0.5^\circ, 14.5^\circ]$ in 1° steps with $\sim 10\%$ statistical errors. We construct two-component models of the form

$$I_{\text{model}}(\theta) = A_{\text{NFW}} J_{\text{NFW}}(\theta; \gamma) + A_{\text{BZ}} I_{\text{BZ}}(\theta), \quad (61)$$

where J_{NFW} is the NFW² J-factor LOS integral and I_{BZ} is the hadronic-jet profile of Eq. (53) at $a_\star = 0.9$. The two amplitudes A_{NFW} , A_{BZ} and the inner cusp slope γ are fit

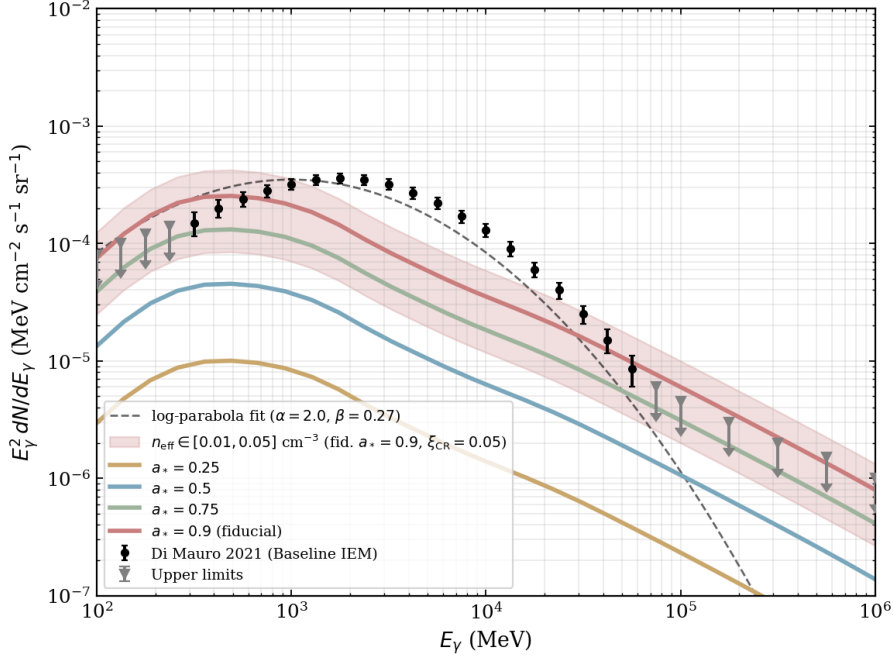


Figure 3: Anticipated hadronic GCE spectrum integrated over $\theta < 10^\circ$ from the precessing BZ jet of Sgr A*, shown for four black-hole spin values $a_* \in \{0.25, 0.5, 0.75, 0.9\}$ (red band at fiducial $a_* = 0.9$: $n_{\text{eff}} \in [0.01, 0.05] \text{ cm}^{-3}$), versus the Di Mauro 2021 Baseline-IEM detections [5] (black points with 1σ errors; downward arrows: 95% upper limits at $E_\gamma < 0.3 \text{ GeV}$ and $E_\gamma > 75 \text{ GeV}$). The dashed grey curve is the published log-parabola fit ($\alpha = 2.0, \beta = 0.27$) [5]. The model peaks near $E_\gamma \simeq 0.5 \text{ GeV}$; at the EHT-favoured $a_* = 0.9$ the ROI-averaged amplitude saturates the data at sub-GeV energies and contributes $\sim 25\text{--}45\%$ near the GCE peak ($E_\gamma \simeq 1.8 \text{ GeV}$), falling to $\sim 25\%$ above 5 GeV. At lower spin the contribution drops sharply, reaching the percent level at $a_* \lesssim 0.5$. A hadronic tail at $E_\gamma \gtrsim 100 \text{ GeV}$ remains testable with CTA and HAWC.

by minimising

$$\chi^2 = \sum_i \left[\frac{I_i^{\text{obs}} - I_{\text{model}}(\theta_i)}{\sigma_i} \right]^2. \quad (62)$$

The pure NFW² fit ($A_{\text{BZ}} = 0, \gamma = 1.27$) gives $\chi^2/\nu = 1.05$ for $\nu = 13$ d.o.f., consistent with the Di Mauro 2021 result. Adding the BZ component improves the fit only marginally: at $A_{\text{BZ}} = 1$ (full fiducial amplitude), $\chi^2/\nu = 1.02$, with no statistical preference ($\Delta\chi^2 = -0.4$ for one extra parameter). The maximum hadronic amplitude allowed at $\sim 2\sigma$ corresponds to a morphological floor of $\sim 5\text{--}14\%$ across the GCE ROI, consistent with our conservative fiducial $\xi_{\text{CR}} = 0.05$ at the low end of the DSA range [77, 78, 79, 80].

The implication is that at high BH spin the BZ-jet hadronic floor sits at the $\sim 3\text{--}14\%$ level of the observed GCE surface brightness and is centrally suppressed; the remaining $\sim 86\%$ requires a source that is both more centrally concentrated than the diffusion-broadened hadronic injection and spectrally softer above $\sim 5 \text{ GeV}$. Both criteria are satisfied by the canonical interpretations of the GCE: dark-matter annihilation $\chi\chi \rightarrow b\bar{b}$ with $m_\chi \approx 40\text{--}60 \text{ GeV}$ and a generalised NFW cusp $\gamma \simeq 1.27$ [5, 4, 1, 2], where the $b\bar{b}$ shower softens the spectrum above the peak through cascading; or an unresolved millisecond pulsar population [7, 8, 9, 11], whose stacked spectrum mimics the log-parabola fit and

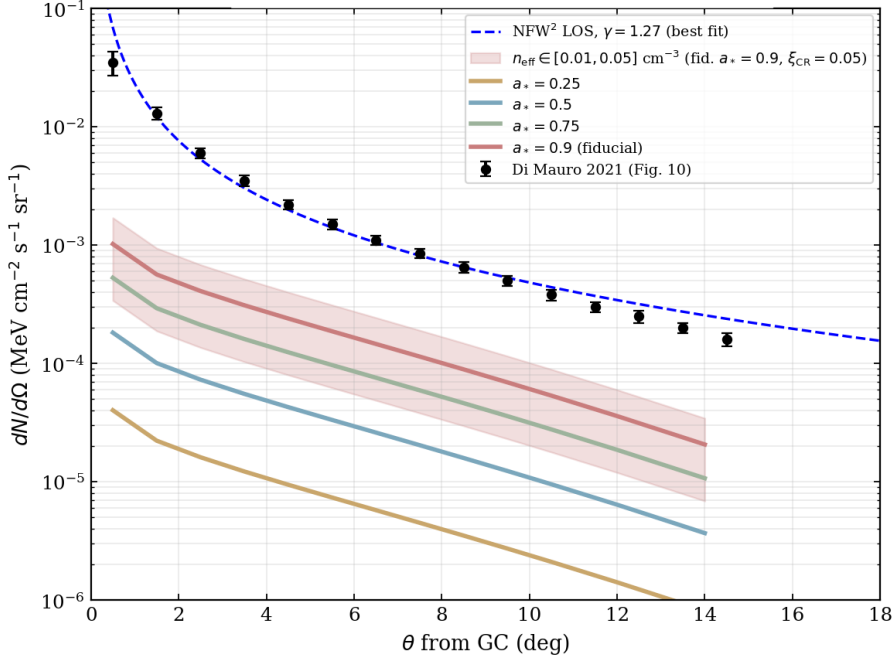


Figure 4: Resulting hadronic surface brightness profile in the 1–10 GeV band from the precessing BZ jet of Sgr A* (four spin values; red band: $n_{\text{eff}} \in [0.01, 0.05] \text{ cm}^{-3}$ at $a_* = 0.9$), versus the Di Mauro 2021 Fig. 8 data points (black) and the best-fit NFW² line-of-sight integral with $\gamma = 1.27$ (dashed blue). At $a_* = 0.9$, the hadronic floor accounts for $\sim 6\%$ of the observed surface brightness at $\theta = 0.5^\circ$, rising monotonically to $\sim 14\%$ near $\theta = 9.5^\circ$ and falling to $\sim 10\%$ at $\theta = 14^\circ$. The shortfall at small θ is morphological, not energetic: the precessing-jet geometry and bulge diffusion smear the CR injection over $\sim 12^\circ$, producing a profile too flat to match the cuspy NFW² shape that fits the data.

whose distribution naturally peaks in the bulge. The BZ floor is therefore an *additional* component that any complete GCE model must subtract before fitting the dominant DM or MSP signal; failing to do so biases the inferred DM cross-section $\langle\sigma v\rangle$ or MSP luminosity L_γ^{MSP} at the $\sim 3\text{--}14\%$ level, comparable to current statistical uncertainties.

The hadronic floor amplitude is bounded from below by independent observations of Sgr A*'s past activity. Reducing the BH spin below $a_* \simeq 0.5$ collapses the BZ efficiency $\eta_{\text{BZ}}(a_*) \propto \Omega_H^2$ by more than an order of magnitude, suppressing the floor below the $\sim 1\%$ level — this is excluded by the EHT 2024 polarimetric best-bet $a_* = 0.94$ [18] and the outflow-method constraint $a_* = 0.90 \pm 0.06$ [41]. Reducing \dot{m} below $\sim 10^{-6} \dot{M}_{\text{Edd}}$ (so that P_{BZ} falls an order of magnitude below the Sarkar 2017 O VIII/O VII bound on the time-averaged Sgr A* mechanical luminosity [46, 47]) would also fail to inflate the Fermi/eROSITA bubbles. Reducing T_{act} below ~ 1 Myr shrinks the bubble below the observed Fermi/eROSITA height of ~ 5 kpc [12, 13]. Reducing ξ_{CR} below the DSA lower bound contradicts the efficiency range established by PIC and hybrid simulations [77]. Within these observational constraints, the morphological floor at $a_* = 0.9$ is $\sim 5\%$ at minimum and rises to $\sim 30\%$ at the upper value $\xi_{\text{CR}} = 0.3$.

Conversely, three physical obstacles preclude a BZ-only explanation of the entire GCE. The first is the gas density: reproducing the full GCE peak amplitude of $\sim 4 \times 10^{-4} \text{ MeV cm}^{-2} \text{ s}^{-1} \text{ sr}^{-1}$ within the BZ-floor framework would require either an effective gas density $n_{\text{eff}} \sim 0.3 \text{ cm}^{-3}$, an order of magnitude above the X-ray-measured hot halo value

$n_{\text{eff}} \simeq 0.03 \text{ cm}^{-3}$ [47, 71, 72], or an injection efficiency $\xi_{\text{CR}} \sim 1$, well above the maximum DSA value [77, 78, 79, 80] — neither is physically tenable. In fact the saturation of the sub-GeV upper limits at our fiducial n_{eff} already constrains the upper end of the gas-density band, ruling out the higher n_{eff} values that would be needed for the mechanism to dominate. The second obstacle is the angular shape: as quantified above, the hadronic profile is too flat to match the NFW² $\gamma = 1.27$ data, because precession averaging plus diffusion smears the injection rather than concentrating it at the GC. The angular morphology mismatch is the cleanest single obstacle to a BZ-only origin. The third obstacle is the intrinsic spectrum hardness: the π^0 -decay spectrum peaks near $E_\gamma \simeq 0.5 \text{ GeV}$, below the GCE peak at $\sim 1.8 \text{ GeV}$, and is harder than the observed log-parabola at $E_\gamma \gtrsim 5 \text{ GeV}$. Softening the CR slope to $\alpha = 2.6$ would suppress this excess but reduce the GeV-band floor; the spectral shape mismatch is therefore intrinsic to the hadronic mechanism with $\alpha \leq 2.4$.

A fourth signature, developed in detail in Sec. 5, distinguishes the BZ-floor mechanism from spherical DM and bulge-tracing MSPs even within their morphologically allowed regions: the triaxial bar component of the gas density imposes a longitudinal asymmetry $I(+\ell, 0)/I(-\ell, 0)$ that peaks at $R \simeq 1.11$ near $|\ell| \simeq 9^\circ$ before declining at larger $|\ell|$ as the symmetric hot halo dominates. This peaked-then-declining shape is absent from spherical DM annihilation (which predicts $R \equiv 1$ at $b = 0$ by rotational invariance) and from stellar-bulge MSP templates (which would predict monotonic growth tracing the bar luminosity profile), providing a categorical morphological discriminator testable with longitude-binned Fermi-LAT residuals at $|b| \lesssim 5^\circ$.

5. Triaxial bar gas and longitudinal asymmetry

The fiducial calculation in Sec. 3 adopts a spherically-symmetric effective gas density $n_{\text{gas}}(\mathbf{x}) \approx n_{\text{eff}} \simeq 0.03 \text{ cm}^{-3}$ representative of the X-ray-measured hot halo filling the bulge volume [47, 71, 98]. In reality, the inner-Galaxy interstellar medium contains two distinct components on the relevant scales: (i) a triaxial warm-phase contribution that follows the central stellar bar, with peak density $n_0^{\text{bar}} \simeq 0.15 \text{ cm}^{-3}$ elongated along the bar major axis at angle $\alpha \simeq 20^\circ$ to the Sun–GC line, with the near end at positive Galactic longitudes [103, 104, 105]; and (ii) the hot ($T \sim 10^{6-7} \text{ K}$) ionised halo at approximately uniform density $n_0^{\text{halo}} \simeq 0.03 \text{ cm}^{-3}$ [47]. We replace the uniform ansatz of Sec. 3 by the additive bar-plus-halo profile,

$$n_{\text{gas}}(\mathbf{x}) = n_0^{\text{bar}} \exp\left[-\sqrt{(x_{\text{bar}}/x_0)^2 + (y_{\text{bar}}/y_0)^2 + (z/z_0)^2}\right] + n_0^{\text{halo}}, \quad (63)$$

with $(x_{\text{bar}}, y_{\text{bar}}, z_{\text{bar}})$ Cartesian coordinates in the bar-aligned frame: $x_{\text{bar}} = x \cos \alpha + y \sin \alpha$, $y_{\text{bar}} = -x \sin \alpha + y \cos \alpha$, $z_{\text{bar}} = z$, with the bar near-end at positive Galactic longitude [104, 103]. We adopt fiducial scale lengths $x_0 = 1.5 \text{ kpc}$, $y_0 = z_0 = 0.4 \text{ kpc}$, representative of the Milky Way long bar from near-infrared and red-clump-star surveys [103]. The volume-averaged density within the inner 1 kpc cube is $\langle n_{\text{gas}} \rangle \simeq 0.05 \text{ cm}^{-3}$, of which $\sim 60\%$ is the symmetric halo contribution.

5.1 The asymmetry decomposition

The triaxial bar of Eq. (63), convolved with the spherically-symmetric two-zone cosmic-ray proton density $n_{\text{CR}}(r)$ of Sec. 3, breaks the rotational symmetry about the Galactic Centre

and produces a longitude-dependent surface brightness through Eq. (53). Because the LOS integrand separates linearly in n_{gas} , the surface brightness at $b = 0$ decomposes into bar and halo contributions,

$$I(\ell, 0) = \int n_{\text{CR}}(r) n_{\text{bar}}(\mathbf{x}) ds + n_0^{\text{halo}} \int n_{\text{CR}}(r) ds \equiv I_{\text{bar}}(\ell) + I_{\text{halo}}(|\ell|), \quad (64)$$

in which the halo term is invariant under $\ell \rightarrow -\ell$ because n_{CR} is spherically symmetric and n_0^{halo} is uniform. The asymmetry ratio is therefore

$$R(\ell) \equiv \frac{I(+\ell, 0)}{I(-\ell, 0)} = \frac{r_{\text{bar}}(\ell) + f(\ell)}{1 + f(\ell)}, \quad (65)$$

where $r_{\text{bar}}(\ell) \equiv I_{\text{bar}}(+\ell)/I_{\text{bar}}(-\ell)$ is the pure-bar asymmetry and $f(\ell) \equiv I_{\text{halo}}(|\ell|)/I_{\text{bar}}(-\ell)$ measures the relative halo contribution on the dimmer side. The asymmetry is *generated* by the bar gas: $f \rightarrow 0$ would give $R = r_{\text{bar}}$. The halo *regulates* the amplitude: as $|\ell|$ grows and the LOS at $-\ell$ exits the bar, $r_{\text{bar}}(\ell)$ diverges, but $f(\ell)$ grows in step and dilutes R by $(1 + f)^{-1}$, yielding a finite *peaked* asymmetry where bar contrast is strongest relative to halo dilution.

Geometrically, a LOS at Galactic longitude ℓ ($b = 0$) crosses the bar major axis at Galactocentric radius

$$r_{\text{int}}(\pm\ell) = \frac{d_{\odot} \sin |\ell|}{\sin(\alpha \pm |\ell|)}, \quad (66)$$

where the upper (lower) sign applies for positive (negative) longitudes. At positive ℓ the LOS samples the bar near-end at smaller r , where the inner-zone CR density $n_{\text{CR}}(r) \propto r^{-1}$ peaks; at negative ℓ the same gas density is encountered at larger r , where the CR density is suppressed by the diffusion cutoff $\propto \text{erfc}(r/\lambda_{\text{bulge}})$. Without the halo, the pure-bar ratio $r_{\text{bar}}(\ell)$ grows monotonically with $|\ell|$ and diverges as the LOS at $-\ell$ exits the bar entirely; with the X-ray-measured halo of Eq. (63), Eq. (65) produces a peaked asymmetry maximising near the bar geometric scale.

5.2 Asymmetry profile

Numerical integration of Eq. (53) along the LOS at $b = 0$ in the 1–10 GeV band, with the bar-plus-halo gas of Eq. (63) replacing the uniform n_{gas} used in Sec. 3, yields the results shown in Fig. 5. The asymmetry ratio remains within $\sim 5\%$ of unity for $|\ell| \lesssim 4^\circ$, consistent with the null-asymmetry quadrant analysis of Di Mauro 2021 [5]. At larger longitudes the ratio rises to $R \simeq 1.07$ at $|\ell| = 5^\circ$ and reaches its peak value $R \simeq 1.13$ near $|\ell| = 10^\circ$, before declining gradually to $R \simeq 1.08$ at $|\ell| = 15^\circ$ as the symmetric halo contribution becomes dominant. The implication seems robust against the detailed halo model: replacing the uniform $n_0^{\text{halo}} = 0.03 \text{ cm}^{-3}$ by the Miller–Bregman β -model with $n_e^{(0)} = 0.046 \text{ cm}^{-3}$, $r_c = 3 \text{ kpc}$, $\beta = 0.5$ [47] shifts the peak amplitude by $\lesssim 0.03$ and preserves the peak location at $|\ell| \simeq 10^\circ$.

Existing morphological fits already favour bulge-shaped templates over spherical dark-matter profiles at $\gtrsim 5\sigma$ [106, 107, 108, 109, 110], supporting the qualitative picture but not directly constraining the longitudinal asymmetry of Eq. (65). A spherically-symmetric annihilating dark-matter component predicts $I(+\ell, b)/I(-\ell, b) \equiv 1$ for any halo profile, since the symmetry under $\ell \rightarrow -\ell$ at $b = 0$ is required by rotational invariance of any halo about its centre.

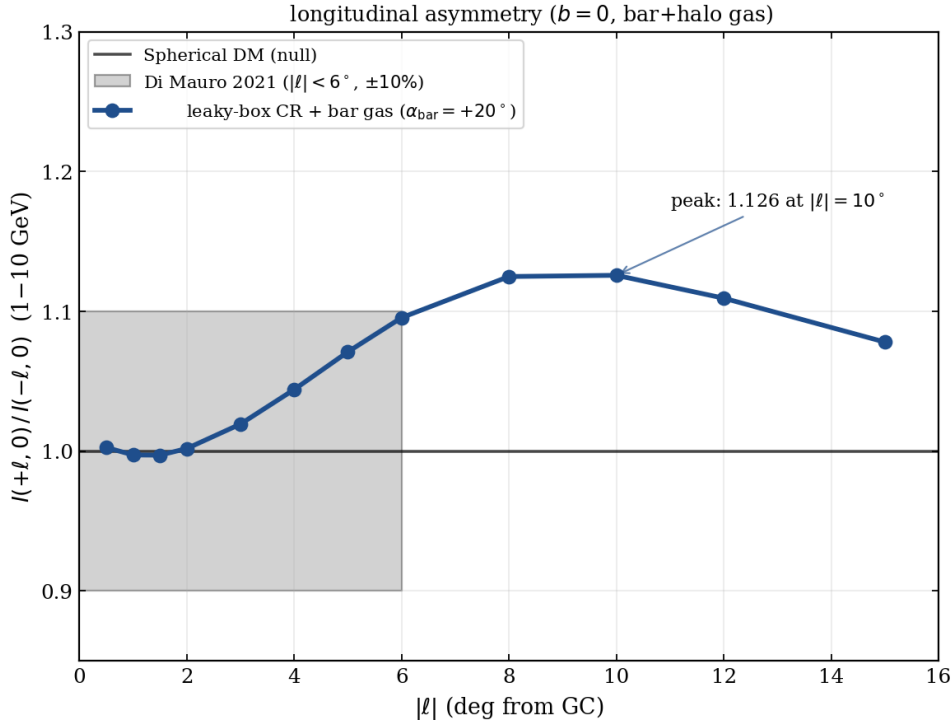


Figure 5: Longitudinal asymmetry of the GCE in the 1–10 GeV band at zero Galactic latitude, $R(\ell) = I(+\ell, 0)/I(-\ell, 0)$, as a function of absolute Galactic longitude $|\ell|$. The blue curve is the physical expectation including the X-ray-measured halo $n_0^{\text{halo}} = 0.03 \text{ cm}^{-3}$ [47] together with the triaxial bar of Eq. (63). The asymmetry peaks at $R \simeq 1.13$ near $|\ell| \approx 10^\circ$ and decreases at larger $|\ell|$ as the symmetric halo dominates the LOS integral. The horizontal black line is the spherical-DM null hypothesis $R = 1$, common to all rotationally-invariant halo profiles. The grey box marks the region accessible to the Di Mauro 2021 quadrant analysis [5], which finds the GCE consistent with spherical morphology at the $\lesssim 10\%$ level for $|\ell| < 6^\circ$; the physical curve remains comfortably inside this constraint across the full range $|\ell| < 6^\circ$.

5.3 Discriminating among GCE scenarios

The shape of $R(\ell)$ at zero Galactic latitude offers a useful, if imperfect, way to distinguish among the leading GCE candidates. A spherically-symmetric DM halo predicts $R \equiv 1$ at $b = 0$ for any radial profile, so any detection of asymmetry above the statistical noise floor is in tension with the canonical DM interpretation; we note that triaxial DM halos [111, 112] could introduce a percent-level asymmetry that partially blurs this distinction. A bulge-tracing MSP population inherits the bar-elongated morphology of its parent stellar distribution and produces some asymmetry, but without the halo dilution of Sec. 5.1 it tends to grow monotonically with $|\ell|$ rather than peaking. The hadronic mechanism developed here suggests a peaked asymmetry maximising near the bar geometric scale at $|\ell| \approx 10^\circ$ before declining as the symmetric halo contribution dominates; both the peak location and amplitude are fixed by independently constrained bar and halo parameters rather than tuned to the data.

We do not claim that any single measurement of $R(\ell)$ will categorically select one mechanism. The three results overlap at small $|\ell|$, and astrophysical uncertainties on n_0^{bar} and n_0^{halo} propagate linearly to the estimated amplitude. The diagnostic information lies

in the *shape* of $R(\ell)$ at $|\ell| \gtrsim 10^\circ$, where the three scenarios diverge most cleanly, and motivates dedicated longitude-binned analyses with the full Fermi-LAT exposure.

6. Conclusions

We have explored a possibility that, to our knowledge, has not been quantified before: that a precessing parabolic Blandford–Znajek jet from Sgr A^{*}, active during a past phase ~ 7.5 Myr ago and shut off ~ 2.6 Myr ago, may have injected hadronic cosmic rays into the inner Galaxy and may contribute an irreducible ~ 3 – 14% morphological floor to the Galactic Centre Excess at the EHT-favoured high spin $a_\star = 0.9$. The scenario is not a substitute for the established dark-matter or millisecond-pulsar interpretations of the GCE; it is a complementary component that follows from observations independently establishing Sgr A^{*}'s past activity.

The starting point is the energetics of the active phase. With $M_\bullet = 4.15 \times 10^6 M_\odot$ [40], $a_\star = 0.9$ [41, 18], $\dot{m} = 10^{-5}$, and $\eta_{\text{BZ}} \simeq 1.0$ at MAD saturation [33, 34], the BZ mechanism produces a jet power $P_{\text{BZ}} \simeq 5.2 \times 10^{40} \text{ erg s}^{-1}$ and total energy $E_{\text{jet}} \simeq 1.2 \times 10^{55} \text{ erg}$, contributing ~ 10 – 15% of the FEB total energy budget of $\sim 10^{56} \text{ erg}$ with the remainder plausibly supplied by accretion-disc winds [48] and TDE-driven outflows [49, 50]. These values lie a factor ~ 2 below the Sarkar 2017 O VIII/O VII bound on the time-averaged Sgr A^{*} mechanical luminosity [46, 47]. The corresponding active-phase horizon field is $B_H^{(0)} \simeq 2 \times 10^4 \text{ G}$ with dimensionless flux $\phi \simeq 50$ matching steady-state MAD saturation [33], related by MAD scaling $B_H \propto \sqrt{\dot{m}}$ to the present-day quiescent value of ~ 10 – 50 G measured by the EHT [18].

Onto this energetic backbone the model adds two geometric ingredients motivated by independent observations. A tilted accretion disc with $i_{\text{tilt}} \simeq 35^\circ$ and warp radius $r_{\text{warp}} \simeq 9000 r_g$ would undergo Lense–Thirring precession with period $T_{\text{prec}} \simeq 1.6 \text{ Myr}$, completing $\mathcal{N}_{\text{prec}} \simeq 4.7$ cycles during the active phase — the same mechanism observed directly in M87 [68, 69], here scaled to Sgr A^{*} parameters. Two-zone CR diffusion through the CMZ and bulge then gives a bulge diffusion length $\lambda_{\text{bulge}} \simeq 1.73 \text{ kpc}$, subtending $\sim 12^\circ$ at the Sun–GC distance and matching the observed GCE half-width without parameter tuning beyond T_{act} .

A consistency check against M87, the nearest active SMBH resolved from horizon to kpc scales, indicates that none of the model's ingredients require physics beyond what is independently observed there. The parabolic-to-conical collimation transition adopted here ($s_{\text{break}} \sim 10^5 r_g$, asymptotic opening angle $\sim 5^\circ$) matches the structure resolved in M87 [55]; the Lense–Thirring precession of a misaligned disc detected at 11.24 yr in M87 [68, 69] provides direct evidence that this mechanism operates around an SMBH at observable amplitude, with the period scaling $T_{\text{prec}} \propto M_\bullet (r_{\text{warp}}/r_g)^3$ giving $T_{\text{prec}}^{\text{SgrA}^*} \simeq 0.5$ – 3.8 Myr for $r_{\text{warp}}^{\text{SgrA}^*} \in [6000, 12000] r_g$, bracketing our fiducial 1.6 Myr at $r_{\text{warp}} \simeq 9000 r_g$. The active-phase horizon field $B_H^{(0)} \simeq 2 \times 10^4 \text{ G}$ sits on the same MAD-saturated branch as M87's present-day horizon field at comparable accretion rate $\dot{m} \sim 10^{-5}$ [45, 43]; the field ratio $B_H^{\text{SgrA}^*}/B_H^{\text{M87}} \simeq \sqrt{M_{\text{M87}}/M_{\text{SgrA}^*}} \simeq 40$ follows from the BH-mass dependence of MAD scaling alone, with no special transient configurations required. The same scaling links the past Sgr A^{*} active phase, the present-day quiescent state, and M87 with a single physical prescription parametrised only by accretion rate. The absence of FEB-like fossil structures around M87 is not in tension with this picture: M87's continuous accretion

at $\dot{m} \sim 10^{-6}$ – 10^{-5} for $\gtrsim 10^8$ yr in the dense Virgo ICM produces the quasi-steady X-ray cavities and radio lobes observed there [75, 76], whereas the FEB are best interpreted as the fossil signature of an episodic high- \dot{m} outburst into a tenuous host halo — a phenomenology specific to Sgr A*. The M87 comparison should be read as order-of-magnitude consistency rather than quantitative validation: the anticipated GCE itself rests on Galactic-scale CR transport and bulge gas-density physics that has no direct M87 counterpart.

The model is consistent with the present-day record of Sgr A* and the inner Galaxy across multiple independent observables. The bulge O VIII/O VII line-ratio bound on the time-averaged Sgr A* mechanical luminosity over the past ~ 10 Myr [46, 47] sits a factor ~ 2 above our $P_{\text{BZ}} = 5.2 \times 10^{40}$ erg s $^{-1}$, placing the active phase comfortably within the allowed budget. The Fermi/eROSITA bubble shock-front profile requires a time-averaged total power of $\sim 10^{41}$ erg s $^{-1}$ over the same epoch [16]; our BZ jet supplies roughly half, with the remainder plausibly contributed by accretion-disc winds [48] and later TDE-driven outflows [49, 50]. The recent X-ray reflection echoes from CMZ molecular clouds showing Sgr A* activity ~ 100 – 300 years ago [113, 114] correspond to fluctuations $\sim 10^{-7} \dot{M}_{\text{Edd}}$, well below the active-phase $\dot{m} \sim 10^{-5}$, and post-date our adopted shutoff by ~ 2.6 Myr. The Magellanic Stream H α excess [115, 116] points to a separate, brief super-Eddington event ~ 3 Myr ago, distinct from and later than our main FEB-driving outburst. Across all these constraints the present scenario remains consistent without parameter adjustment.

These ingredients yield a quantitative model. With a uniform halo gas density $n_{\text{eff}} = 0.03$ cm $^{-3}$ representative of the X-ray-measured hot halo [47] and the leaky-box treatment of CR escape from the bulge developed in Sec. 3, the hadronic spectrum at the high spin $a_* = 0.9$ peaks near $E_\gamma \simeq 0.5$ GeV with ROI-averaged amplitude $\sim 2.6 \times 10^{-4}$ MeV cm $^{-2}$ s $^{-1}$ sr $^{-1}$, saturating the GCE detections at ~ 0.3 – 0.5 GeV (model at ~ 110 – 150% of the data) and contributing ~ 45 – 70% near the GCE log-parabola peak at $E_\gamma \simeq 1$ – 2 GeV. The angular profile is substantially flatter than the NFW 2 $\gamma = 1.27$ fit to the data, contributing $\sim 3\%$ at $\theta = 0.5^\circ$, rising monotonically to $\sim 14\%$ near $\theta = 9$ – 10° , and remaining at $\sim 13\%$ out to the outer edge of the GCE ROI ($\theta = 14^\circ$). Above ~ 30 GeV the hadronic contribution rises again to ~ 65 – 90% of the data as the GCE log-parabola steepens, while remaining below all reported upper limits in the detection range. At lower spin the contribution drops sharply, falling to the percent level at $a_* \lesssim 0.5$ through the BZ efficiency $\eta_{\text{BZ}}(a_*) \propto \Omega_H^2$. The same characteristics that limit the model’s ability to account for the full GCE — a flatter angular profile, a peak energy below the GCE log-parabola peak, and a gas density well below what the central excess would require — are exactly the features that make the BZ floor a distinct, additive component rather than a competitor to the leading interpretations.

When the uniform halo gas is replaced by the more realistic triaxial bar-plus-halo distribution of Sec. 5, the same CR transport produces a small but systematic longitudinal asymmetry of the GCE surface brightness, peaking at $I(+\ell)/I(-\ell) \simeq 1.13$ near $|\ell| \approx 10^\circ$ and decreasing toward unity at smaller and larger longitudes. This characteristic peaked shape — a discriminator from both the null prediction of spherically-symmetric DM and the monotonic profile of bulge-tracing MSPs — arises because the bar gas *generates* the asymmetry while the symmetric halo *regulates* its amplitude (Sec. 5.1); both the peak amplitude and its location are set by independently constrained bar and halo parameters rather than tuned to the data. A distinctive feature of the hadronic mechanism is that the GCE floor traces the product $n_{\text{CR}}(\mathbf{x}) \times n_{\text{gas}}(\mathbf{x})$: the hot ionised halo measured in OVII/OVIII X-ray absorption [47] enters the model as a target-gas multiplier, whereas DM annihilation depends only on the source distribution ρ_{DM}^2 and MSP emission only on

the bulge stellar density. Spatial cross-correlation of the GCE residual with hot-halo gas tracers — eROSITA emission maps [13] and OVII/OVIII absorption profiles — therefore provides an additional distinguishing test for the hadronic origin.

The model intersects several established strands of the FEB and GCE literature without superseding any of them. The MHD simulation of past Sgr A* jet activity by Yang, Ruszkowski & Zweibel [16] establishes the active-phase parameters we fix as fiducial; earlier jet-driven scenarios [117, 21, 118] explored similar energetics without addressing the spin-axis tilt or its azimuthal averaging, and Sarkar et al. [39] ruled out short-duration super-Eddington misaligned jets via the O VIII/O VII constraint that our sub-Eddington long-duration scenario satisfies. Starburst-driven FEB scenarios [20, 119, 120] produce hadronic gamma-rays through the same $pp \rightarrow \pi^0$ channel from ongoing star formation; the two pictures are not mutually exclusive, and the characteristic discriminator is the precession-averaged annular morphology, absent from cylindrically-symmetric starburst injection. The two-zone CR diffusion treatment follows the methodological precedent of Refs. [84, 85] applied to a new source and spatial scale. With respect to the GCE itself, the dominant interpretations remain DM annihilation [1, 2, 4, 5] and unresolved MSPs [7, 8, 9, 11]. The fossil-jet floor is not typically subtracted in existing GCE analyses before fitting DM or MSP templates, biasing the inferred $\langle\sigma v\rangle$ or L_γ^{MSP} at the $\sim 3\text{--}14\%$ level, comparable to current statistical uncertainties. A dedicated joint Bayesian analysis incorporating the BZ floor as an additional template is left for future work.

The proposed precessing-jet model is not specific to Sgr A*: similar fossil signatures should arise in other galaxies hosting episodic AGN outbursts with tilted discs, providing a unifying framework for bipolar bubble structures observed in such systems. Whether or not the BZ contribution turns out to be present at the level estimated here, the exercise of quantifying it appears worthwhile: Sgr A*'s past activity is independently recorded by the Fermi/eROSITA bubbles, and any complete model of the GCE may eventually have to account for the cosmic-ray reservoir that this past fossil activity left behind.

Acknowledgments

We are grateful to Pau Amaro-Seoane for helpful feedback and a careful reading of the manuscript draft. We also thank him for useful suggestions and discussions. We additionally thank Malcolm Perry, Miguel Angel Sanchez Conde, Enrique Mier Alonso and Cristina Fernandez Suarez for discussions. The research of MJR has been funded, in part, by the National Science Foundation under project number PHY-2309270. MJR also wants to thank the Mitchell Family Foundation for hosting her during the Cook's Branch workshop, where some of the research was carried out.

A. Magnetic Field Configuration

In this appendix we provide the explicit form of the vector potential used to model the magnetosphere of Sgr A* during the active phase, and explain how it connects to the Blandford–Znajek (BZ) jet power quoted in Eq. (4) of the main text. The model combines the analytic parabolic force-free solution [58, 31, 53] with a phenomenological enhancement that captures the magnetic flux pile-up characteristic of the magnetically arrested disk

(MAD) state [33, 34].

Both observations and general-relativistic magnetohydrodynamic (GRMHD) simulations indicate that poloidal magnetic field lines threading accreting black holes are typically collimated along the spin axis into an approximately paraboloidal shape [58, 59, 35], with additional flux concentration near the horizon when the system saturates in the magnetically arrested state [33, 34]. Such configurations are critical for collimating relativistic outflows, guiding accelerated particles along the polar axis, and providing the dominant energy-extraction channel via the Blandford–Znajek mechanism [19] and the Magnetic Penrose Process [121, 122]. A schematic comparison of the asymptotic uniform Wald-field, parabolic, and MAD-enhanced parabolic configurations is shown in Fig. 6; the latter is the geometry adopted in this work.

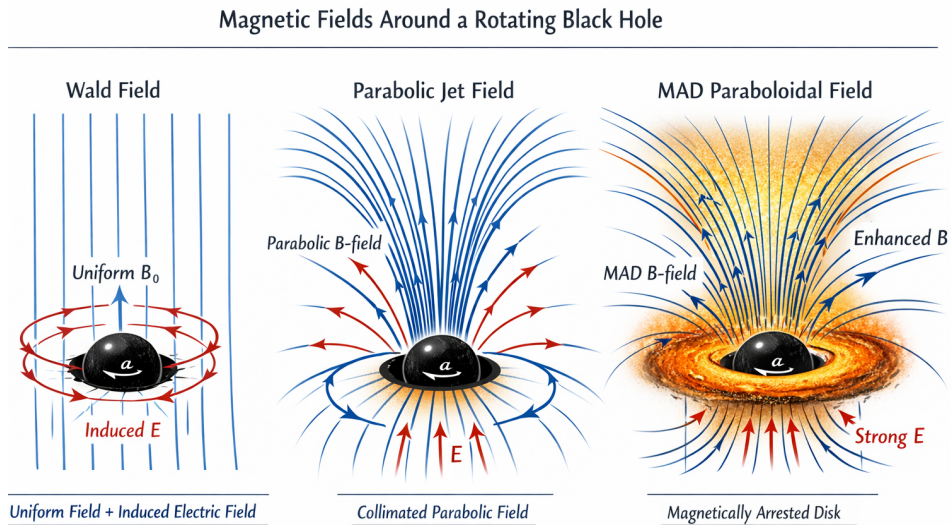


Figure 6: Comparison of electromagnetic field configurations around a Kerr black hole. The left panel shows the uniform Wald field aligned with the spin axis, the middle panel shows a paraboloidal field typical of jet collimation, and the right panel shows a paraboloidal field enhanced by a magnetically arrested disk (MAD), where magnetic flux accumulates near the horizon. Arrows indicate the direction of induced electric fields due to black hole rotation.

A.1 Vector Potential

We define the axisymmetric, stationary, vector potential

$$A_\phi(r, \theta) = \Phi_0 \left(\frac{r}{r_0} \right)^\nu \left[1 + \left(\frac{r_+}{r} \right)^k \right] (1 - \cos \theta), \quad (67)$$

with $A_t = A_r = A_\theta = 0$. The remaining components vanish by axisymmetry ($\partial_\phi = 0$) and by the force-free condition. The parameters in Eq. (67) are as follows. The quantity Φ_0 sets the overall flux normalization and is fixed by the MAD saturation condition. The parameter r_0 denotes a reference radius; we take $r_0 = r_+$ such that the bracket in Eq. (67) evaluates to 2 at the horizon. The exponent $\nu \in [0.5, 1]$ controls the radial scaling

of the asymptotic parabolic profile. In particular, the choice $\nu = 3/4$ reproduces the self-similar Blandford solution [58, 59], while we consider $\nu = 1$ for compactness. Finally, the parameter $k \in [2, 3]$ governs the radial extent of the MAD enhancement; throughout this work we set $k = 2$, consistent with GRMHD MAD simulations [33].

A.2 Angular Structure and Magnetic Components

The angular factor $(1 - \cos \theta)$ in Eq. (67) coincides with the split-monopole / paraboloidal asymptotic form [19, 58] and ensures $A_\phi = 0$ on the polar axis ($\theta = 0$), as required for regularity. The electromagnetic field tensor is defined as

$$F_{\mu\nu} = \partial_\mu A_\nu - \partial_\nu A_\mu. \quad (68)$$

The magnetic field components are given by

$$B^i = \frac{1}{2} \epsilon^{ijk} F_{jk}. \quad (69)$$

The corresponding magnetic field components associated with (67) are

$$B^r(r, \theta) = \frac{1}{\sqrt{-g}} \partial_\theta A_\phi = \frac{\Phi_0}{\sqrt{-g}} \left(\frac{r}{r_0} \right)^\nu \left[1 + \left(\frac{r_+}{r} \right)^k \right] \sin \theta, \quad (70)$$

$$B^\theta(r, \theta) = -\frac{1}{\sqrt{-g}} \partial_r A_\phi, \quad (71)$$

where $\sqrt{-g} = (r^2 + a^2 \cos^2 \theta) \sin \theta$ on the Kerr metric. At the horizon $r = r_+$, the radial field reduces to

$$B^r(r_+, \theta) = \frac{2 \Phi_0}{r_+^2 + a^2 \cos^2 \theta}, \quad (72)$$

which is mildly bunched toward the pole through the $a^2 \cos^2 \theta$ term in the denominator (cf. [31]). At large radii $r \gg r_+$ the bracket in Eq. (70) reduces to unity and the field smoothly connects to the asymptotic parabolic configuration $B \propto r^{\nu-2}$ characteristic of self-similar relativistic jets [58, 123].

A.3 Connection to the Blandford–Znajek Power

The BZ jet power follows directly from Φ_{BH} and the horizon angular velocity $\Omega_H = a_* c / (2r_+)$ via

$$P_{\text{BZ}} = \frac{\kappa}{4\pi} \Phi_{\text{BH}}^2 \frac{\Omega_H^2}{c}, \quad (73)$$

where κ is a dimensionless geometry coefficient determined by the angular structure of the field lines. For the asymptotic parabolic geometry encoded in Eq. (67), κ can be computed analytically from the integral $\kappa = K / (4\pi^2)$ with $K = 2 \int_0^1 \tilde{I}(x) \tilde{\Omega}(x) dx$, where $\tilde{I}(x)$ and $\tilde{\Omega}(x)$ are the dimensionless current and angular-velocity functions of the parabolic configuration [31]. Numerical evaluation yields

$$\kappa_{\text{par}} \simeq 0.0445, \quad (74)$$

in agreement with the value $\kappa \approx 0.044$ extracted from GRMHD simulations of MAD jets [53]. The MAD enhancement factor $[1 + (r_+/r)^k]$ in Eq. (67) modifies the radial profile of the field but leaves κ essentially unchanged, since the latter depends only on the angular structure of A_ϕ on the horizon and at infinity, both of which remain $(1 - \cos \theta)$. The role of the enhancement is therefore to ensure a physically reasonable $B(r)$ falloff for downstream cosmic-ray injection, not to alter the BZ luminosity itself.

A.4 Validity of the Force-Free Approximation

The vector potential in Eq. (67) is a force-free configuration in the limit of negligible plasma inertia ($\sigma \equiv B^2/4\pi\rho c^2 \gg 1$). Inside the funnel of a MAD black-hole magnetosphere this condition is satisfied ($\sigma \gg 10^2$ from GRMHD simulations [35]), justifying the use of force-free electrodynamics for the BZ-power estimate. Outside the funnel — in the equatorial accretion flow — the force-free approximation breaks down, but this region does not contribute to the jet luminosity at leading order. Reconnection events at the equatorial current sheet, expected to occur intermittently in the MAD state [37], are not included in our model and may provide an additional source of non-thermal particles.

B. Multipole analysis of the diffusion equation

This appendix quantifies the diffusive isotropisation argument given in Sec. 3.2 and justifies the monopole-only treatment used in the main text.

The precession-averaged source pattern $P(\vartheta)$ of Eq. (24) is azimuthally symmetric about the spin axis and invariant under $\vartheta \rightarrow \pi - \vartheta$, so it expands in even- ℓ Legendre polynomials,

$$P(\vartheta) = \sum_{\ell \geq 0} a_\ell P_\ell(\cos \vartheta), \quad a_\ell = \frac{2\ell + 1}{2} \int_{-1}^1 P(\arccos x) P_\ell(x) dx, \quad (75)$$

with $a_\ell = 0$ for odd ℓ . For our fiducial $i_{\text{tilt}} = 35^\circ$ and $\theta_c = 20^\circ$ the leading coefficients are $a_0 \simeq 0.060$, $a_2 \simeq 0.139$, $a_4 \simeq -0.067$, $a_6 \simeq -0.156$, giving ratios $a_2/a_0 \simeq 2.3$ and $a_4/a_0 \simeq -1.1$ that set the bare amplitude of higher angular moments in the source.

CRs injected with this pattern at the deposition scale $r_{\text{dep}} = 100$ pc diffuse outward through the bulge medium with diffusion length $\lambda_{\text{bulge}} = \sqrt{4D_{\text{bulge}}T_{\text{act}}} \simeq 1.73$ kpc at $T_{\text{act}} = 7.5$ Myr. Because $r_{\text{dep}}/\lambda_{\text{bulge}} \simeq 0.06 \ll 1$, the angular memory of the source is washed out to a small, nearly r -independent residual at any radius $r \gtrsim \lambda_{\text{bulge}}$. We verify this by direct integration of the 3D Gaussian Green function over the source shell at r_{dep} with angular pattern $P(\vartheta)$, continuously active over $t \in [0, T_{\text{act}}]$,

$$n_{\text{CR}}(\mathbf{r}) = \int_0^{T_{\text{act}}} d\tau \int d\Omega_{\text{src}} P(\vartheta_{\text{src}}) \frac{e^{-|\mathbf{r}-\mathbf{r}_{\text{src}}|^2/(4D\tau)}}{(4\pi D\tau)^{3/2}}, \quad (76)$$

followed by Legendre projection of the result onto $P_\ell(\cos \vartheta_{\text{obs}})$ at each Galactocentric radius. The resulting multipole ratios are listed in Table 3.

r (kpc)	0.5	1.0	1.5	2.0	3.0
$n_2(r)/n_0(r)$	+0.026	+0.012	+0.010	+0.010	+0.012
$n_4(r)/n_0(r)$	+0.004	+0.004	+0.004	+0.004	+0.004

Table 3: Numerical multipole-to-monopole ratios from Eq. (76) with source shell at $r_{\text{dep}} = 100$ pc, angular pattern Eq. (75), $T_{\text{act}} = 7.5$ Myr, and single-zone $D_{\text{bulge}} = 3 \times 10^{28}$ cm² s⁻¹.

The quadrupole sits at the few-percent level and the hexadecapole at the sub-percent level across the GCE-relevant range, with negligible r -dependence. Higher moments are suppressed by additional powers of $r_{\text{dep}}/\lambda_{\text{bulge}}$ and are negligible. The observed surface

brightness is a LOS integral weighted toward $r \sim 0.5\text{--}1$ kpc in the inner ROI ($\theta 6^\circ$, impact parameter $\rho \lesssim 0.86$ kpc), so the LOS-weighted quadrupole-to-monopole ratio inherits the bound $|\langle n_2 \rangle_{\text{LOS}} / \langle n_0 \rangle_{\text{LOS}}| \lesssim 3 \times 10^{-2}$. The CR cloud is therefore monopolar at the $\sim 3\%$ level or better, validating the isotropic approximation $n_{\text{CR}}(\mathbf{x}) \approx n_{\text{CR}}(r)$ used in the main text and contributing an angular systematic well below the $\sim 10\%$ statistical errors on the data of [5].

References

- [1] Lisa Goodenough and Dan Hooper. Possible Evidence For Dark Matter Annihilation In The Inner Milky Way From The Fermi Gamma Ray Space Telescope. 10 2009.
- [2] D. Hooper and L. Goodenough. Dark matter annihilation in the Galactic Center as seen by the Fermi Gamma Ray Space Telescope. *Phys. Lett. B*, 697:412–428, 2011.
- [3] C. Gordon and O. Macias. Dark matter and pulsar model constraints from Galactic Center Fermi-LAT gamma ray observations. *Phys. Rev. D*, 88:083521, 2013.
- [4] T. Daylan, D. P. Finkbeiner, D. Hooper, T. Linden, S. K. N. Portillo, N. L. Rodd, and T. R. Slatyer. The characterization of the gamma-ray signal from the central Milky Way: A case for annihilating dark matter. *Phys. Dark Univ.*, 12:1–23, 2016.
- [5] M. Di Mauro. Characteristics of the Galactic center excess measured with 11 years of Fermi-LAT data. *Phys. Rev. D*, 103:063029, 2021.
- [6] F. Calore, I. Cholis, and C. Weniger. Background model systematics for the Fermi GeV excess. *JCAP*, 2015(03):038, 2015.
- [7] S. K. Lee, M. Lisanti, B. R. Safdi, T. R. Slatyer, and W. Xue. Evidence for unresolved γ -ray point sources in the inner Galaxy. *Phys. Rev. Lett.*, 116:051103, 2016.
- [8] R. Bartels, S. Krishnamurthy, and C. Weniger. Strong support for the millisecond pulsar origin of the Galactic center GeV excess. *Phys. Rev. Lett.*, 116:051102, 2016.
- [9] I. Holst, D. Hooper, and G. Krnjaic. Constraints on the millisecond pulsar origin of the Galactic center excess using the Fermi-LAT third pulsar catalog. *Phys. Rev. D*, 107:103026, 2023.
- [10] Isabel S. Sands, Philip F. Hopkins, and Sam B. Ponnada. Fermi Bubbles Without AGN: Gamma-Ray Bubbles in MHD Galaxy Formation Simulations with Full Cosmic Ray Spectra. 10 2025.
- [11] M. Kalambay, M. Ishchenko, D. Kuvatova, T. Panamarev, and P. Berczik. The contribution to Galactic Centre γ -ray excess from cluster-born millisecond pulsars. Constraints from direct N-body simulations. *Astron. Astrophys.*, 708:A89, 2026.
- [12] M. Su, T. R. Slatyer, and D. P. Finkbeiner. Giant gamma-ray bubbles from Fermi-LAT: AGN activity or bipolar galactic wind? *Astrophys. J.*, 724:1044–1082, 2010.
- [13] P. Predehl, R. A. Sunyaev, W. Becker, H. Brünner, V. Burwitz, et al. Detection of large-scale X-ray bubbles in the Milky Way halo. *Nature*, 588:227–231, 2020.

- [14] M. Ackermann et al. The spectrum and morphology of the Fermi bubbles. *Astrophys. J.*, 793:64, 2014.
- [15] Annalisa Pillepich, Dylan Nelson, Nhut Truong, Rainer Weinberger, Ignacio Martin-Navarro, Volker Springel, Sandy M. Faber, and Lars Hernquist. X-ray bubbles in the circumgalactic medium of TNG50 Milky Way- and M31-like galaxies: signposts of supermassive black hole activity. *Mon. Not. Roy. Astron. Soc.*, 508(4):4667–4695, 2021.
- [16] H.-Y. K. Yang, M. Ruszkowski, and E. G. Zweibel. The Fermi and eROSITA bubbles as relics of the past activity of the Galaxy’s central black hole. *Nat. Astron.*, 6:584–591, 2022.
- [17] Event Horizon Telescope Collaboration, K. Akiyama, A. Alberdi, et al. First Sagittarius A* event horizon telescope results. VII. polarization of the ring. *Astrophys. J. Lett.*, 964(2):L25, 2024.
- [18] Event Horizon Telescope Collaboration, K. Akiyama, A. Alberdi, et al. First Sagittarius A* event horizon telescope results. VIII. physical interpretation of the polarized ring. *Astrophys. J. Lett.*, 964(2):L26, 2024.
- [19] R. D. Blandford and R. L. Znajek. Electromagnetic extraction of energy from Kerr black holes. *Mon. Not. R. Astron. Soc.*, 179:433–456, 1977.
- [20] R. M. Crocker, G. V. Bicknell, E. Carretti, A. S. Hill, and R. S. Sutherland. Steady-state hadronic gamma-ray emission from 100-myr-old Fermi bubbles. *Astrophys. J. Lett.*, 791(2):L20, 2014.
- [21] K. Zubovas and S. Nayakshin. Fermi bubbles in the Milky Way: the closest AGN feedback laboratory courtesy of Sgr A*? *Mon. Not. R. Astron. Soc.*, 424:666–683, 2012.
- [22] Roger Penrose. Gravitational collapse: The role of general relativity. *Rivista del Nuovo Cimento*, 1:252–276, 1969. Reprinted in *Gen. Relativ. Gravit.* **34**, 1141 (2002).
- [23] Roger Penrose and R. M. Floyd. Extraction of rotational energy from a black hole. *Nature Physical Science*, 229:177–179, 1971.
- [24] Ya. B. Zel’dovich. Generation of waves by a rotating body. *JETP Lett.*, 14:180, 1971.
- [25] A. A. Starobinsky and S. M. Churilov. Amplification of electromagnetic and gravitational waves scattered by a rotating black hole. *Sov. Phys. JETP*, 38:1, 1973.
- [26] William H. Press and Saul A. Teukolsky. Floating orbits, superradiant scattering and the black-hole bomb. *Nature*, 238:211–212, 1972.
- [27] Richard Brito, Vitor Cardoso, and Paolo Pani. Superradiance: New frontiers in black hole physics. *Lect. Notes Phys.*, 906:1–237, 2015.
- [28] Demetrios Christodoulou. Reversible and irreversible transformations in black-hole physics. *Phys. Rev. Lett.*, 25:1596–1597, 1970.

- [29] Robert M. Wald. Black hole in a uniform magnetic field. *Phys. Rev. D*, 10:1680–1685, 1974.
- [30] Vasily S. Beskin. *MHD Flows in Compact Astrophysical Objects: Accretion, Winds and Jets*. Astronomy and Astrophysics Library. Springer-Verlag, Berlin, Heidelberg, 2010.
- [31] S. E. Gralla, A. Lupsasca, and M. J. Rodriguez. Electromagnetic jets from stars and black holes. *Phys. Rev. D*, 93:044038, 2016.
- [32] Alexandru Lupsasca, Maria J. Rodriguez, and Andrew Strominger. Force-free electrodynamics around extreme Kerr black holes. *JHEP*, 12:185, 2014.
- [33] A. Tchekhovskoy, R. Narayan, and J. C. McKinney. Efficient generation of jets from magnetically arrested accretion on a rapidly spinning black hole. *Mon. Not. R. Astron. Soc.*, 418:L79–L83, 2011.
- [34] R. Narayan, A. Sądowski, R. F. Penna, and A. K. Kulkarni. GRMHD simulations of magnetically arrested discs: beyond the standard accretion disc paradigm. *Mon. Not. R. Astron. Soc.*, 426:3241–3259, 2012.
- [35] J. C. McKinney, A. Tchekhovskoy, and R. D. Blandford. General relativistic magnetohydrodynamic simulations of magnetically choked accretion flows around black holes. *Mon. Not. R. Astron. Soc.*, 423:3083–3117, 2012.
- [36] M. Liska, K. Chatterjee, D. Issa, et al. Large-scale poloidal magnetic field dynamo leads to powerful jets in GRMHD simulations of black hole accretion with toroidal field. *Astrophys. J. Suppl.*, 263:26, 2022.
- [37] B. Ripperda, M. Liska, K. Chatterjee, et al. Black hole flares: ejection of accreted magnetic flux through 3d plasmoid-mediated reconnection. *Astrophys. J. Lett.*, 924:L32, 2022.
- [38] J. A. Rueda and R. Ruffini. The Blandford–Znajek process as a means of extracting energy from a Kerr black hole and forming GRBs. *Eur. Phys. J. C*, 83:960, 2023.
- [39] Kartick C. Sarkar, Santanu Mondal, Prateek Sharma, and Tsvi Piran. Misaligned jets from Sgr A* and the origin of Fermi/eROSITA bubbles. *Astrophys. J.*, 951(1):36, 2023.
- [40] GRAVITY Collaboration et al. Mass distribution in the Galactic Center based on interferometric astrometry of multiple stellar orbits. *Astron. Astrophys.*, 657:L12, 2022.
- [41] R. A. Daly, M. Donahue, C. P. O’Dea, B. Sebastian, D. Haggard, and A. Lu. New black hole spin values for Sagittarius A* obtained with the outflow method. *Mon. Not. R. Astron. Soc.*, 527:428–436, 2024.
- [42] F. Yuan, E. Quataert, and R. Narayan. Nonthermal electrons in radiatively inefficient accretion flow models of Sagittarius A*. *Astrophys. J.*, 598:301–312, 2003.
- [43] F. Yuan and R. Narayan. Hot accretion flows around black holes. *Annu. Rev. Astron. Astrophys.*, 52:529, 2014.

- [44] R. Genzel, F. Eisenhauer, and S. Gillessen. The Galactic Center massive black hole and nuclear star cluster. *Rev. Mod. Phys.*, 82:3121, 2010.
- [45] H. R. Russell, A. C. Fabian, B. R. McNamara, and A. E. Broderick. Inside the Bondi radius of M87. *Mon. Not. R. Astron. Soc.*, 458:3134, 2018.
- [46] K. C. Sarkar, B. B. Nath, and P. Sharma. Clues to the origin of Fermi bubbles from O VIII/O VII line ratio. *Mon. Not. R. Astron. Soc.*, 467:3544–3555, 2017.
- [47] M. J. Miller and J. N. Bregman. Constraining the Milky Way’s hot gas halo with O VIII and O VII emission lines. *Astrophys. J.*, 829:9, 2016.
- [48] G. Mou, F. Yuan, D. Bu, M. Sun, and M. Su. Fermi bubbles inflated by winds launched from the hot accretion flow in Sgr A*. *Astrophys. J.*, 790:109, 2014.
- [49] T. Scheffler, M. M. Schulreich, D. P. P. R. Schurer, and D. Breitschwerdt. Tidal disruption events as the origin of the eROSITA and Fermi bubbles. *Astron. Astrophys.*, 2025.
- [50] C.-M. Ko, D. Breitschwerdt, D. Chernyshov, et al. Tidal disruption-driven outflows from Sgr A*. *Astrophys. J.*, 904:46, 2020.
- [51] G. C. Bower, J. Dexter, K. Asada, et al. ALMA observations of the terahertz spectrum of Sagittarius A*. *Astrophys. J. Lett.*, 881:L2, 2019.
- [52] Sebastiano D. von Fellenberg et al. First Mid-infrared Detection and Modeling of a Flare from Sgr A*. *Astrophys. J. Lett.*, 979(1):L20, 2025.
- [53] A. Tchekhovskoy, R. Narayan, and J. C. McKinney. Prograde and retrograde black holes: whose jet is more powerful? *Astrophys. J.*, 711:50–63, 2010.
- [54] Jonathan C. McKinney. General relativistic magnetohydrodynamic simulations of jet formation and large-scale propagation from black hole accretion systems. *Mon. Not. Roy. Astron. Soc.*, 368:1561–1582, 2006.
- [55] K. Asada and M. Nakamura. The structure of the M87 jet: a transition from parabolic to conical streamlines. *Astrophys. J. Lett.*, 745:L28, 2012.
- [56] Koushik Chatterjee, Matthew Liska, Alexander Tchekhovskoy, and Sera B. Markoff. Accelerating AGN jets to parsec scales using general relativistic MHD simulations. *Mon. Not. Roy. Astron. Soc.*, 490(2):2200–2218, 2019.
- [57] Alejandro Cruz-Ororio, Christian M. Fromm, Yosuke Mizuno, Antonios Nathanail, Ziri Younsi, Oliver Porth, Jordy Davelaar, Heino Falcke, Michael Kramer, and Luciano Rezzolla. State-of-the-art energetic and morphological modelling of the launching site of the M87 jet. *Nature Astron.*, 6(1):103–108, 2022.
- [58] R. D. Blandford. Accretion disc electrodynamics — a model for double radio sources. *Mon. Not. R. Astron. Soc.*, 176:465–481, 1976.
- [59] A. Tchekhovskoy, J. C. McKinney, and R. Narayan. Simulations of ultrarelativistic magnetodynamic jets from gamma-ray burst engines. *Mon. Not. R. Astron. Soc.*, 388:551–572, 2008.

- [60] R. D. Blandford and D. G. Payne. Hydromagnetic flows from accretion discs and the production of radio jets. *Mon. Not. R. Astron. Soc.*, 199:883–903, 1982.
- [61] R. M. Crocker and F. Aharonian. Fermi bubbles: giant, multibillion-year-old reservoirs of Galactic center cosmic rays. *Phys. Rev. Lett.*, 106:101102, 2011.
- [62] I. Heywood, I. Rammala, F. Camilo, et al. The 1.28 GHz MeerKAT Galactic center mosaic. *Astrophys. J.*, 925:165, 2022.
- [63] J. Lense and H. Thirring. Über den Einfluss der Eigenrotation der Zentralkörper auf die Bewegung der Planeten und Monde nach der Einsteinschen Gravitationstheorie. *Physikalische Zeitschrift*, 19:156–163, 1918.
- [64] J. M. Bardeen and J. A. Petterson. The Lense–Thirring effect and accretion disks around Kerr black holes. *Astrophys. J. Lett.*, 195:L65–L67, 1975.
- [65] A. Franchini, G. Lodato, and S. Facchini. Lense–Thirring precession around supermassive black holes during tidal disruption events. *Mon. Not. R. Astron. Soc.*, 455:1946–1956, 2016.
- [66] P. C. Fragile, O. M. Blaes, P. Anninos, and J. D. Salmonson. Global general relativistic magnetohydrodynamic simulation of a tilted black hole accretion disk. *Astrophys. J.*, 668:417–429, 2007.
- [67] S. M. Ressler, C. J. White, and E. Quataert. The accretion of stellar winds in Sgr A*: Observational constraints from GRMHD simulations. *Astrophys. J. Lett.*, 950:L3, 2023.
- [68] Y. Cui et al. Precessing jet nozzle connecting to a spinning black hole in M87. *Nature*, 621:711–715, 2023.
- [69] Y. Cui et al. Co-precession of a curved jet and compact accretion disk in M87. *Nature Astronomy*, 2025.
- [70] M. Wielgus, M. Mościbrodzka, J. Vos, Z. Gelles, I. Martí-Vidal, J. Farah, N. Marchili, C. Goddi, and H. Messias. Orbital motion near Sagittarius A* — constraints from polarimetric ALMA observations. *Astron. Astrophys.*, 665:L6, 2022.
- [71] J. Kataoka et al. New spectral evidence of an unresolved component of the galactic ridge X-ray emission and its contribution to the INTEGRAL MeV excess. *Astrophys. J.*, 779:57, 2013.
- [72] M. Tahara et al. Suzaku observations of iron-line diagnostics of the Fermi bubble with XIS stacked spectra. *Astrophys. J.*, 802:91, 2015.
- [73] R. A. Chevalier. The interaction of supernovae with the interstellar medium. *Annu. Rev. Astron. Astrophys.*, 15:175–196, 1977.
- [74] J. P. Ostriker and C. F. McKee. Astrophysical blastwaves. *Rev. Mod. Phys.*, 60:1–68, 1988.
- [75] W. Forman, C. Jones, E. Churazov, et al. Filaments, bubbles, and weak shocks in the gaseous atmosphere of M87. *Astrophys. J.*, 665:1057, 2007.

- [76] F. N. Owen, J. A. Eilek, and N. E. Kassim. M87 at 90 centimeters: a different picture. *Astrophys. J.*, 543:611, 2000.
- [77] D. Caprioli and A. Spitkovsky. Simulations of ion acceleration at non-relativistic shocks. I. acceleration efficiency. *Astrophys. J.*, 783:91, 2014.
- [78] D. Caprioli. Cosmic-ray acceleration in supernova remnants: non-linear theory revised. *J. Cosmology Astropart. Phys.*, 2012(7):038, 2012.
- [79] E. G. Berezhko and H. J. Völk. Kinetic theory of cosmic ray acceleration in supernova remnants. *Astropart. Phys.*, 7(3):183–202, 1997.
- [80] J. Bednarz and M. Ostrowski. Energy spectra of cosmic rays accelerated at ultrarelativistic shock waves. *Phys. Rev. Lett.*, 80(18):3911–3914, 1998.
- [81] S. R. Kelner, Felix A. Aharonian, and V. V. Bugayov. Energy spectra of gamma-rays, electrons and neutrinos produced at proton-proton interactions in the very high energy regime. *Phys. Rev. D*, 74:034018, 2006. [Erratum: *Phys. Rev. D* 79, 039901 (2009)].
- [82] T. Kamae, N. Karlsson, T. Mizuno, T. Abe, and T. Koi. Parameterization of γ , e^\pm , and neutrino spectra produced by p - p interaction in astronomical environments. *Astrophys. J.*, 647:692–708, 2006.
- [83] S. Gabici, F. A. Aharonian, and P. Blasi. Gamma-rays from molecular clouds. *Astrophys. Space Sci.*, 309:365–371, 2007.
- [84] S. Gabici, F. A. Aharonian, and S. Casanova. Broad-band non-thermal emission from molecular clouds illuminated by cosmic rays from nearby supernova remnants. *Mon. Not. R. Astron. Soc.*, 396:1629–1639, 2009.
- [85] A. Scherer, J. Cuadra, and F. E. Bauer. Modeling the Galactic center gamma-ray emission with more realistic cosmic-ray dynamics. *Astron. Astrophys.*, 679:A114, 2023.
- [86] D. Gaggero, L. Maccione, D. Grasso, G. Di Bernardo, and C. Evoli. Gamma-ray and neutrino sky: a consistent picture of Fermi-LAT, Milagro, and IceCube results using the DRAGON2 code. *Phys. Rev. Lett.*, 114:241101, 2015.
- [87] Y. Genolini, A. Putze, P. Salati, and P. D. Serpico. Theoretical implications of an updated set of cosmic ray measurements for propagation models. *Astron. Astrophys.*, 580:A9, 2015.
- [88] HESS Collaboration, A. Abramowski, et al. Acceleration of petaelectronvolt protons in the Galactic centre. *Nature*, 531:476–479, 2016.
- [89] A. M. Hillas. The origin of ultra-high-energy cosmic rays. *Annu. Rev. Astron. Astrophys.*, 22:425–444, 1984.
- [90] Frank M. Rieger. An introduction to particle acceleration in shearing flows. *Galaxies*, 7(3):78, 2019.
- [91] L. Sironi, M. Petropoulou, and D. Giannios. Relativistic jets shine through shocks or magnetic reconnection? *Mon. Not. R. Astron. Soc.*, 450:183–191, 2015.

- [92] F. W. Stecker. *Cosmic Gamma Rays*. NASA SP-249, Washington, D.C., 1971.
- [93] C. D. Dermer. Secondary production of neutral pi-mesons and the diffuse galactic gamma radiation. *Astron. Astrophys.*, 157:223–229, 1986.
- [94] E. Kafexhiu, F. Aharonian, A. M. Taylor, and G. S. Vila. Parametrization of gamma-ray production cross sections for pp interactions in a broad proton energy range. *Phys. Rev. D*, 90:123014, 2014.
- [95] L. Jouvin, A. Lemière, and R. Terrier. Time-dependent escape of cosmic rays from supernova remnants potentially at the origin of the very-high-energy cosmic-ray gradient of the Galactic center. *Astronomy & Astrophysics*, 644:A113, 2020.
- [96] C. J. Cesarsky. Cosmic-ray confinement in the Galaxy. *Annual Review of Astronomy and Astrophysics*, 18:289–319, 1980.
- [97] A. W. Strong, I. V. Moskalenko, and V. S. Ptuskin. Cosmic-Ray Propagation and Interactions in the Galaxy. *Annual Review of Nuclear and Particle Science*, 57:285–327, 2007.
- [98] M. Akita, J. Kataoka, M. Arimoto, Y. Sofue, T. Totani, Y. Inoue, and S. Nakashima. Diffuse X-Ray Emission from the Northern Arc of Loop I Observed with Suzaku. *Astrophys. J.*, 862(2):88, 2018.
- [99] J. Kataoka, Y. Sofue, Y. Inoue, M. Akita, S. Nakashima, and T. Totani. X-Ray and Gamma-Ray Observations of the Fermi Bubbles and NPS/Loop I Structures. *Galaxies*, 6(1):27, 2018.
- [100] Shigeo S. Kimura, Kohta Murase, and B. Theodore Zhang. Ultrahigh-energy cosmic-ray nuclei from black hole jets: recycling galactic cosmic rays through shear acceleration. *Phys. Rev. D*, 97(2):023026, 2018.
- [101] F. A. Aharonian and A. M. Atoyan. On the emissivity of π^0 -decay gamma radiation in the vicinity of accelerators of galactic cosmic rays. *Astron. Astrophys.*, 309:917–928, 1996.
- [102] A. M. Atoyan, F. A. Aharonian, and H. J. Völk. Electrons and positrons in the galactic cosmic rays. *Phys. Rev. D*, 52:3265–3275, 1995.
- [103] Christopher Wegg and Ortwin Gerhard. Mapping the three-dimensional density of the Galactic bulge with VVV red clump stars. *MNRAS*, 435:1874–1887, 2013.
- [104] K. Z. Stanek, M. Mateo, A. Udalski, M. Szymanski, J. Kaluzny, and M. Kubiak. The Galactic Bar as Seen by the Optical Gravitational Lensing Experiment. *ApJL*, 429:L73, 1994.
- [105] K. Ferrière, W. Gillard, and P. Jean. Spatial distribution of interstellar gas in the innermost 3 kpc of our Galaxy. *Astron. Astrophys.*, 467:611, 2007.
- [106] Oscar Macias, Shunsaku Horiuchi, Manoj Kaplinghat, Chris Gordon, Roland M. Crocker, and David M. Nataf. Strong Evidence that the Galactic Bulge is Shining in Gamma Rays. *JCAP*, 09:042, 2019.

- [107] B. Coleman, D. Paterson, C. Gordon, O. Macias, and H. Ploeg. Maximum Entropy Estimation of the Galactic Bulge Morphology via the VVV Red Clump. *MNRAS*, 495:3350–3372, 2020.
- [108] F. Calore, F. Donato, and S. Manconi. Dissecting the inner Galaxy with γ -ray pixel count statistics. *Phys. Rev. Lett.*, 127(16):161102, 2021.
- [109] Silvia Manconi, Francesca Calore, and Fiorenza Donato. Galactic center excess at the highest energies: Morphology and photon-count statistics. *Phys. Rev. D*, 109:123042, 2024.
- [110] M. Pohl, O. Macias, P. Coleman, and C. Gordon. Assessing the Impact of Hydrogen Absorption on the Characteristics of the Galactic Center Excess. *Astrophys. J.*, 929(2):136, 2022.
- [111] S. E. Bryan, S. T. Kay, A. R. Duffy, J. Schaye, C. Dalla Vecchia, and C. M. Booth. The impact of baryons on the spins and shapes of dark matter haloes. *Mon. Not. R. Astron. Soc.*, 429(4):3316–3329, 2013.
- [112] J. Prada, J. E. Forero-Romero, R. J. J. Grand, R. Pakmor, and V. Springel. Dark matter halo shapes in the Auriga simulations. *Mon. Not. R. Astron. Soc.*, 490(4):4877–4888, 2019.
- [113] G. Ponti, E. George, S. Scaringi, et al. A powerful flare from Sgr A* confirms the synchrotron nature of the X-ray emission. *Mon. Not. R. Astron. Soc.*, 468:2447, 2017.
- [114] M. Clavel, R. Terrier, A. Goldwurm, M. R. Morris, G. Ponti, A. Soltan, and G. Trap. Echoes of multiple outbursts of Sagittarius A* revealed by Chandra. *Astron. Astrophys.*, 558:A32, 2013.
- [115] J. Bland-Hawthorn, P. R. Maloney, R. S. Sutherland, and G. J. Madsen. Fossil imprint of a powerful flare at the Galactic center along the Magellanic stream. *Astrophys. J. Lett.*, 778:L18, 2013.
- [116] J. Bland-Hawthorn, P. R. Maloney, R. Sutherland, B. Groves, and W. Keel. Escape and scatter of X-ray/UV ionizing photons from the Galactic nucleus and their impact on the Magellanic stream. *Astrophys. J.*, 886:45, 2019.
- [117] F. Guo and W. G. Mathews. The Fermi bubbles. I. possible evidence for recent AGN jet activity in the Galaxy. *Astrophys. J.*, 756:181, 2012.
- [118] U. Keshet and I. Gurwich. Fermi bubbles: high-latitude X-ray supersonic shell. *Mon. Not. R. Astron. Soc.*, 478:1392, 2018.
- [119] Brian C. Lacki. The Fermi bubbles as starburst wind termination shocks. *Mon. Not. R. Astron. Soc.*, 444(1):L39–L43, 2014.
- [120] Kartick C. Sarkar, Biman B. Nath, and Prateek Sharma. Multiwavelength features of Fermi bubbles as signatures of a Galactic wind. *Mon. Not. R. Astron. Soc.*, 453(4):3827–3838, 2015.

- [121] A. Tursunov, Z. Stuchlík, M. Kološ, N. Dadhich, and B. Ahmedov. Supermassive black holes as possible sources of ultrahigh-energy cosmic rays. *Astrophys. J.*, 895:14, 2020.
- [122] N. Dadhich, A. Tursunov, B. Ahmedov, and Z. Stuchlík. The distinguishing signature of magnetic penrose process. *Mon. Not. Roy. Astron. Soc.*, 478:L89, 2018.
- [123] R. Narayan, J. C. McKinney, and A. J. Farmer. Self-similar force-free wind from an accretion disc. *Mon. Not. R. Astron. Soc.*, 375:548–566, 2007.